Embedding a One-column Ocean Model (SIT 1.06) in the Community Atmosphere Model 5.3 (CAM5.3; CAM5–SIT v1.0) to Improve Madden–Julian Oscillation Simulation in Boreal Winter

Yung-Yao Lan, Huang-Hsiung Hsu*, Wan-Ling Tseng, and Li-Chiang Jiang

Research Center for Environmental Changes, Academia Sinica, Taipei 11529, Taiwan

*Correspondence to: Huang-Hsiung Hsu (hhhsu@gate.sinica.edu.tw)

Abstract

The effect of the air–sea interaction on the Madden–Julian Oscillation (MJO) was investigated using the one-column ocean model Snow–Ice–Thermocline (SIT 1.06) embedded in the Community Atmosphere Model 5.3 (CAM5.3; hereafter CAM5–SIT v1.0). The SIT model with 41 vertical layers was developed to simulate sea surface temperature (SST) and upper-ocean temperature variations with a high vertical resolution that resolves the cool skin and diurnal warm layer and the upper oceanic mixed layer. A series of 30-year sensitivity experiments were conducted in which various model configurations (e.g., coupled versus uncoupled, vertical resolution and depth of the SIT model, coupling domains, and absence of the diurnal cycle) were considered to evaluate the effect of air–sea coupling on MJO simulation. Most of the CAM5–SIT experiments exhibit higher fidelity than the CAM5-alone experiment in characterizing the basic features of the MJO such as spatiotemporal variability and the eastward propagation in boreal winter. The overall MJO simulation performance of CAM5–SIT benefits from (1) better resolving the fine vertical structure of upper-ocean temperature and therefore the air–sea interaction that result in more realistic intraseasonal variability in both SST and atmospheric circulation and (2) the adequate thickness of a vertically-gridded ocean mixed layer. The sensitivity experiments demonstrate the necessity of coupling the tropical eastern Pacific in addition to the tropical Indian Ocean and the tropical western Pacific. Coupling is more essential in the south than north of the equator in the tropical western Pacific. Enhanced MJO could be obtained without considering the diurnal cycle in coupling.

1. Introduction

The Madden–Julian Oscillation (MJO) is a tropical large-scale convection circulation system that propagates eastward across the warm pool region from the tropical Indian Ocean (IO) to the western Pacific (WP) on an intraseasonal time scale (Madden and Julian, 1972). The MJO is not just an atmospheric phenomenon. The findings from a multi-nation field campaign called the Dynamics of MJO/Cooperative Indian Ocean Experiment on Intraseasonal Variability in the Year 2011 (DYNAMO/CINDY2011; de Szoeke et al., 2017; Johnson and Ciesielski, 2017; Pujiana et al., 2018; Yoneyama et al., 2013; Zhang and Yoneyama, 2017) revealed vigorous air–sea coupling during the evolution of the MJO (Chang et al., 2019; DeMott et al., 2015; Jiang et al., 2015, 2020; Kim et al., 2010; Li et al., 2016; Li et al., 2020; Newman et al., 2009; Pei et al., 2018; Tseng et al., 2014). During the suppression of convection, the MJO propagates eastward with light winds, which is accompanied by enhanced downwelling shortwave radiation absorption, weaker upward latent and sensible fluxes, less cloudiness and precipitation, and weaker vertical mixing in the upper ocean, thus causing an increase in the upper-ocean temperature. In the following active phase when deep convection occurs, downwelling shortwave radiation is reduced and stronger westerly winds enhance latent/sensible heat flux (LHF/SHF) loss from the ocean surface, thus causing a decrease in the upper-ocean temperature (DeMott et al., 2015; Madden and Julian, 1972, 1994; Zhang, 2005).

In addition to the ocean surface, the structure of the upper ocean also evolves. Alappattu et al. (2017) reported that during an MJO event, surface flux perturbations cause changes in the ocean thermohaline structure, thus affecting the mixed-layer temperature. The following change in sea surface temperature (SST) can further affect atmospheric circulation of the MJO. Variations in SST mediate LHF and SHF

exchange across the air–sea interface. Although SST responds to atmospheric forcing, the modulation of LHF and SHF provides feedback to the atmosphere (DeMott et al., 2015; Jiang et al., 2020). Li et al. (2008, 2020) proposed that the phase relationship between SST and convection implies a delayed air–sea interaction mechanism whereby a preceding active-phase MJO may trigger an inactive-phase MJO through the delayed effect of the induced SST anomaly over the IO. The reduction in SST caused by a preceding active-phase MJO may, in turn, yields delayed ocean feedback that initiates a suppressed-phase MJO, and vice versa. The by-no-means negligible effect of intraseasonal SST variations caused by surface heat fluxes suggests that the ocean state can affect the MJO (DeMott et al., 2015, 2019; Hong et al., 2017; Li et al., 2020).

Since its discovery almost five decades ago, the MJO remains a phenomenon that poses a challenge to the capacity of state-of-the-art atmospheric general circulation models (AGCMs) such as those participating in the Coupled Model Intercomparison Project phase 5 and 6 to generate successful simulations (Ahn et al., 2017, 2020; Bui and Maloney 2018; Jiang et al., 2020; Hung et al., 2013; Kim et al., 2011).

Recent studies have reported that air–sea coupling improves the representation of the MJO in numerical simulation (Bernie et al., 2008; Crueger et al., 2013; DeMott et al., 2015; Li et al., 2016; Li et al., 2020; Tseng et al., 2014; Woolnough et al., 2007). Tseng et al. (2014) indicated that effectively resolving the upper-ocean warm layer to capture temperature variations in the upper few meters of the ocean could improve MJO simulation. DeMott et al. (2015) suggested that the tropical atmosphere–ocean interaction may sustain or amplify the pattern of the enhanced and suppressed atmospheric convection of the eastward propagation. DeMott et al. (2019) demonstrated that the improved MJO eastward propagation in four coupled models

84 resulted from enhanced low-level convective moistening for a rainfall rate of >5 mm
85 day^{-1} due to air–sea coupling. In addition, numerical experiments have been
86 performed to investigate the effect of the diurnal cycle on the MJO (Hagos et al.,
87 2016; Oh et al., 2013), with the results suggesting that the strength and propagation of
88 the MJO through the Maritime Continent (MC) were enhanced when the diurnal cycle
89 was ignored.
90 Although previous studies have demonstrated the importance of considering the
91 air–sea interaction in a numerical model to improve MJO simulation, additional
92 details regarding model configuration (e.g., vertical resolution and depth of the ocean
93 mixed layer, coupling domain, and absence of the diurnal cycle in air-sea coupling)
94 have not been systematically explored. Tseng et al. (2014) coupled the one-column
95 ocean model Snow–Ice–Thermocline (SIT; Tu and Tsuang, 2005) to the fifth
96 generation of the ECHAM AGCM (ECHAM5–SIT) and indicated that a vertical
97 resolution of 1 m was essential to yield an improved simulation of the MJO with a
98 realistic strength and eastward propagation speed.
99 In this study, we coupled the SIT model to the Community Atmosphere Model
100 version 5.3 (CAM5.3; Neale et al., 2012)—the atmosphere component of the
101 Community Earth System Model version 1.2.2 (CESM1.2.2; Hurrell et al., 2013)—to
102 explore the improvement of MJO simulation by coupling SIT model to another
103 AGCM is reproducible in modeling science. The CAM5.3, which has been widely
104 used for the long-term simulation of the climate system, could not efficiently simulate
105 the eastward propagation of the MJO; instead, the model simulated a tendency for the
106 MJO to move westward in the IO (Boyle et al., 2015, Jiang et al, 2015). By contrast,
107 the updated CESM2 with the new CAM6 could realistically simulate the MJO (Ahn et
108 al., 2020; Danabasoglu et al., 2020). Thus, the well-explored CAM5, which does not
109 produce a realistic MJO, appears to be a favorable choice for exploring coupling a

simple one-dimensional (1-D) ocean model, such as the SIT model, can improve MJO simulation, as well as the effects of model configuration on the degree of the improvement. Such a study can also enhance our understanding regarding the effect of air–sea coupling on the MJO.

The MJO that exhibits a more substantial eastward propagation in boreal winter than in other seasons was the targeted feature in this study. To examine the sensitivity of MJO simulations to different configurations of air-sea coupling, we conducted a series of 30-year numerical experiments by considering various model configurations (e.g., coupled versus uncoupled, vertical resolution and depth of the SIT model, coupling domains, and absence of the diurnal cycle) to investigate the effect of air–sea coupling. This paper is organized as follows. Section 2 describes the data for validation, the model used for simulation, and the design of numerical experiments. Section 3 describes the effect of various air-sea coupling configurations on the MJO simulation determined through detailed MJO diagnostics. Discussion and conclusions are provided in Section 4.

2. Data, methodology, model description, and experimental designs

2.1 Data and methodology

The data analyzed in this study include precipitation from the Global Precipitation Climatology Project (GPCP), outgoing longwave radiation (OLR) and daily SST (Optimum Interpolation SST; OISST) from the National Oceanic and Atmosphere Administration (NOAA), and parameters from the ERA-Interim (ERA-I) reanalysis (Adler et al., 2003; Dee et al., 2011; Lee et al., 2011; Reynolds and Smith, 1995; Schreck et al., 2018). The SST data for the SIT model were obtained from the Hadley Centre Sea Ice and Sea Surface Temperature dataset (Rayner et al., 2003; HadISST1) and the ocean subsurface data (40-layer climatological ocean temperature,

salinity, and currents) for nudging were retrieved from the National Centers for Environmental Prediction (NCEP) Global Ocean Data Assimilation System (GODAS; Behringer and Xue, 2004).

We used the CLIVAR MJO Working Group diagnostics package (CLIVAR, 2009) and a 20–100-day filter (Kaylor, 1977; Wang et al., 2014) to determine intraseasonal variability. MJO phases were defined following the index (namely, RMM1 and RMM2) proposed by Wheeler and Hendon (2004), which considers the first two principal components of the combined near-equatorial OLR and zonal winds at 850 and 200 hPa. The band-passed filtered data were used for calculating the index and defining phases.

2.2 Model description

2.2.1 CAM5.3

The CAM5.3 used in this study has a horizontal resolution of 1.9° latitude × 2.5° longitude and 30 vertical levels with the model top at 0.1 hPa. The MJO could not be realistically simulated in the CAM5.3. Boyle et al. (2015) demonstrated that although making the deep convection dependent on SST improved the simulation of the MJO variance, it exerted a significant negative effect on the mean-state climate of low-level cloud and absorbed shortwave radiation. By comparing the simulation results of an uncoupled and coupled CAM5.3, Li et al. (2016) suggested that air–sea coupling and the convection scheme most significantly affected the MJO simulation in the climate model.

2.2.2 1-D high-resolution TKE ocean model

The 1-D high-resolution turbulence kinetic energy (TKE) ocean model SIT was used to simulate the diurnal fluctuation of SST and surface energy fluxes (Lan et al.,

2010; Tseng et al., 2014; Tu and Tsuang, 2005). The model was well verified against in situ measurements on board the R/V Oceanographic Research Vessel 1 and 3 over the South China Sea (Lan et al., 2010) and on R/V Vickers over the tropical WP (Tu and Tsuang, 2005).

The SIT model determines the vertical profiles of the temperature and momentum of a water column from the surface down to the seabed, except in the fixed ocean model bottom experiment. The default setting of vertical discretization (e.g., in the control coupled experiment) is 41 layers with 12 layers in the first 10.5 m, 6 layers between 10.5 m and 107.8 m (Supplementary Information I). In the 1-D TKE ocean model, temperature and salinity below 107.8 m, where vertical mixing is greatly weakened, are nudged toward the climatological values of GODAS data until 4607 m. The extra high vertical resolution is needed to catch detailed temporal variation of upper ocean temperature characterized by the warm layer and cool skin (Tu and Tsuang, 2005). To account for the neglected horizontal advection heat flux, the ocean is weakly nudged (by using a 30-day time scale) between 10.5 m and 107.8 m and strongly nudged (by using a 1-day time scale) below 107.8 m according to the NCEP GODAS climatological ocean temperature. No nudging is performed within the upper-most 10.5 m. The SIT model calculates twice for each CAM5 time step (30 min; i.e., coupling 48 times per day).

2.3 Experimental design

A series of 30-year numerical experiments (Table 1) were conducted to investigate the effect of the air–sea interaction on the MJO simulation. The HadSST1 used to force the coupled and uncoupled model was the climatological monthly-mean SST averaged over 1982-2001. The monthly SST was linearly interpolated to daily SST fluctuation that forced the model. The SST in air–sea coupling region was

recalculated by the SIT during the simulation, while the prescribed annual cycle of SST was used in the areas outside the coupling region. Ocean bathymetry of the SIT was derived from the NOAA ETOPO1 data (Amante and Eakins, 2009) and interpolated into 1.9° × 2.5° horizontal resolution.

All simulations were driven by the prescribed annual cycle of SST repeatedly for 30 years. The strategy is to evaluate the simulation capacity of climate models under the same condition without considering interannual variation induced by SST. This approach has been widely adopted in many studies (Delworth et al., 2006; Haertel et al., 2020; Subramanian et al., 2011; Tseng et al., 2014; Wang et al., 2005).

Atmospheric initial conditions and external forcing such as CO_2, ozone, and aerosol in near-equilibrium climate state around the year 2000 were taken from F_2000_CAM5 component set based on CESM1.2.2 framework development. The data has been commonly used in present-day simulations using CAM5 (e.g., He et al., 2017).

The setup of five sets of experiment conducted in this study are described as follows.

(1) A standalone CAM5.3 simulation forced by climatological monthly HadISST1 (A–CTL) and the control experiment of coupled CAM5–SIT simulation (C–30NS; 41 vertical levels, coupling in the entire tropics between 30°N and 30°S with a diurnal cycle).

(2) Upper-ocean vertical resolution experiment: Two simulations with the first layer centering at 12 m (C–LR12m) and 34 m (C–LR34m). Further details of the experimental design are shown in supplementary Fig. S1.

(3) Shallow ocean bottom experiment: Three simulations with the ocean model bottom at 10 m (C–HR1mB10m), 30 m (C–HR1mB30m), and 60 m (C–HR1mB60m) (supplementary Fig. S2).

(4) Regional coupling experiment: Four simulations with the coupling region in 0°N–30°N (C–0_30N) and 0°S–30°S (C–0_30S) for latitudinal effect, and 30°E–180°E (C–30_180E) and 30°E–75°W (C–30E_75W) for longitudinal effect. The coupling domains are shown in Fig. 1.

(5) A non-diurnal simulation (C–30NS–nD) that considers the air–sea interaction only once a day, namely, calculating SHF and LHF based on daily mean atmospheric variables and SST. To prevent the inconsistent local time in different regions, the coupling frequency at each grid point remained 48 times per day using the same daily means of atmospheric variables and SST at that particular point. In contrast, the control simulation calculates air-sea fluxes 48 times a day based on instantons values. A comparison between the non-diurnal simulation and the control simulation reveals the effect of diurnal cycle in air0sea coupling.

3. Results and Discussion

The realistic simulation of the MJO has always been a major bottleneck in the development of climate models. In this section, we demonstrate the sensitivity of air–sea coupling experiments using a 1-D high-resolution ocean model significantly improves the MJO simulation by the CAM5.3. The period between November and April when the MJO is the most prominent was the targeted season in this study.

3.1 Improvement of MJO simulation through air–sea coupling

This subsection compares the MJO simulation of the control coupled experiment (C–30NS) with that of the uncoupled AGCM (A–CTL) forced by climatological monthly SST of HadISST1 to demonstrate the effect of air–sea coupling on the MJO simulation by coupling the SIT model to the CAM5.3 in the tropical belt (30°N–30°S).

240

241 **3.1.1 Wavenumber–frequency spectra and eastward propagation characteristics**

242 A wavenumber–frequency spectrum (W–FS) analysis was conducted to quantify
243 propagation characteristics simulated in different experiments. The spectra
244 of unfiltered U850 in ERA-I reanalysis, C–30NS, and A–CTL are shown in Fig. 2a–c,
245 respectively. The C–30NS considering the coupling in 30ºN–30ºS realistically
246 simulates eastward-propagating signals at zonal wavenumber 1 and 30–80-day
247 periods (Fig. 2a–b), although with a slightly larger amplitude compared with ERA-I.
248 By contrast, the uncoupled A–CTL does not yield realistic simulation; instead, it
249 simulates both eastward (wavenumber 1)- and westward (wavenumber 2)-propagating
250 signals with an unrealistic spectral shift to time scales longer than 30–80-day.

251 The major features of the simulated MJO propagation were examined. Figure
252 2d–f show the time evolution of precipitation and U850 anomalies in Hovmöller
253 diagrams, which represent lagged correlation coefficients between the precipitation
254 averaged over 10°S–5°N, 75–100°E and the precipitation and U850 averaged over
255 10°N–10°S on intraseasonal timescales. Figure 2d indicates eastward propagation for
256 both precipitation and U850 from the eastern IO to the dateline, with precipitation
257 leading U850 by approximately a quarter of a cycle. The Hovmöller diagram derived
258 from the C–30NS (Fig. 2e) exhibits the key characteristics of eastward propagation
259 for both precipitation and U850 and the relative phases between the two, although the
260 simulated correlation is slightly weaker than that derived from GPCP and ERA-I. By
261 contrast, the uncoupled A–CTL simulates intraseasonal signals that propagate
262 westward over the IO and weak and much slower eastward propagation crossing the
263 MC and WP (Fig. 2f). The contrast between Fig. 2e and 2f demonstrate that coupling
264 a 1-D TKE ocean model alone could lead to a significant improvement in an AGCM
265 in simulating the major characteristics (e.g., amplitude, propagation direction and

speed, and phase relationship between precipitation and circulation) of the MJO.

3.1.2 Coherence of the simulated MJO

Cross-spectral analysis was conducted to examine the coherence and phase lag between tropical circulation and convection, which were plotted over the tropical wave spectra. Figure 2g–i show the symmetric part (e.g., Wheeler and Kiladis, 1999) of OLR and U850 in ERA-I/NOAA data, C–30NS, and A–CTL, respectively. We present only the spectra between 0 to 0.35 day^{-1} to highlight the MJO and equatorial Kelvin waves. The most prominent characteristics seen in ERA-I/NOAA data are the peak coherence at wavenumbers 1–3 and a phase lag of approximately 90° in the 30–80-day band (Ren et al., 2019; Wheeler and Kiladis 1999). The coupled experiment C–30NS simulates strong coherence in this low-frequency band (wavenumber 1) and exhibits a realistic phase lag relationship between U850 and OLR perturbations. However, the coherence at wavenumbers 2–3 for the 30–80-day period simulated by C–30NS is weaker than that in ERA-I/NOAA data. This undersimulation was also noted in CCSM4 (Subramanian et al., 2011), the uncoupled and coupled CAM4 and CAM5 (Li et al., 2016), and NorESM1-M (Bentsen et al., 2013), which had a version of the CAM as an AGCM. In summary, C–30NS considering the coupling between 30ºN–30ºS produces coherent and energetic patterns in the eastward-propagating intraseasonal fluctuations of U850 and OLR in the tropical IO and WP that are generally consistent with the MJO characteristics. By contrast, the MJO characteristics in A–CTL are considerably weaker than those in C–30NS and that in ERA-I/NOAA data.

3.1.3 Horizontal and vertical structures of the MJO across the MC

Figure 2j–o show the horizontal and vertical structures of the MJO when deep

convection is the strongest over the MC (i.e., phase 5). Figure 2j–l present the 20–100-day filtered OLR (W m^{-2}, shaded) and 850-hPa wind (m s^{-1}, vector). C–30NS realistically simulated the enhanced tropical convection over the eastern IO and the Kelvin-wave-like easterly anomalies over the tropical WP despite undersimulating the convection over the MC (Fig. 2j and 2k). By contrast, A–CTL failed to simulate the enhanced convection over the eastern IO and MC; instead, it simulated considerably weaker convection and easterly winds over the MC and WP, respectively, than that in ERA-I/NOAA data (Fig. 2j and 2l).

Figure 2m–o show the vertical–longitudinal profiles of 20–100-day filtered 15°N–15°S averaged vertical velocity (OMEGA; Pa s^{-1}, shaded) and moist static energy (MSE) anomalies (W m^{-2}, contour) at phase 5. The spatial distribution of negative OMEGA (ascending motion) anomalies generally agreed with OLR anomalies in C–30NS simulation and NOAA data over the Indo-Pacific region (Fig. 2m and 2n). The relatively spatial relationship between the ascending motion and MSE seen in ERA-I is well simulated in the coupled experiment C–30NS. For example, positive MSE anomalies on the eastern side of the anomalous ascent demonstrate that the energy recharge process occurs in advance of the MJO convection over the lower-tropospheric easterlies (Fig. 2m and 2n), whereas negative MSE anomalies on the western side reveal that the discharge process occurs during and after convection over the lower-tropospheric westerlies. By contrast, this phase relationship, considered to be an essential feature leading to the eastward propagation of an MJO (Hannah and Maloney 2014; Heath et al., 2021), is not properly simulated in the uncoupled experiment A–CTL (Fig. 2o), in which the simulated weak negative OMEGA is located between negative and positive MSE anomalies over weak lower-tropospheric wind anomalies and associated with weak convection over the MC (Fig. 2l).

318 The temporal evolution of NOAA OLR and ERA-I U850 (Fig. 3a) indicates
319 that convection originating in the western IO is enhanced during its eastward
320 propagation to the MC where it reaches the peak amplitude and then gradually
321 weakened when continuing moving eastward to the dateline. In the coupled
322 experiment C–30NS, this evolution of convectively coupled circulation is realistically
323 simulated, although it is weaker than the strength seen in NOAA OLR (Fig. 3b).
324 Moreover, the split of convection into two cells off the equator in phase 6 is
325 appropriately simulated in C–30NS (P6 in Fig. 3a and 3b). This split was caused by
326 the topographic and land–sea contrast effects of the MC (Tseng et al., 2017).
327 Associated with the split is the southward detouring of the anomalous convection
328 during the passage of the MJO through the MC (Kim et al. 2017, Tseng et al., 2017;
329 Wu and Hsu, 2009). After the passage of the MJO through the MC, the anomalous
330 convection stays south of the equator and continues moving eastward to the
331 dateline. In the uncoupled A–CTL, the systematic eastward propagation of
332 convectively coupled MJO circulation from the IO into the MC is not simulated.
333 Instead, the convection over the MC develops in situ at a later stage than that
334 observed (e.g., P6 in Fig. 3c) and dissipated rapidly. The A–CTL simulates a pair of
335 off-equator convection anomalies in the eastern IO during phase 2 (P2 in Fig. 3c) that
336 moves westward toward the central IO and were amplified at later stages (e.g., P4 in
337 Fig. 3c). This unrealistic evolution explains the westward propagation tendency
338 observed in the Hovmöller diagram (Fig. 2f).
339
340 **3.1.4 Characteristics of air–sea interaction**
341 Figure 4a–c show the longitude–phase diagram in which the 20–100-day filtered
342 precipitation (shaded) and SST (contour) anomalies were averaged over 10°S–10°N to
343 determine the relationship between precipitation and SST fluctuations and to establish

a link between air–sea coupling and convection. The propagation of the enhanced convection with positive SST anomalies to the east could be clearly seen in GPCP/OISST and the coupled experiment C–30NS (Fig. 4a and 4b). The highest SST anomaly (SSTA) leads the maximum precipitation anomaly by approximately 2–3 phases, and the SSTA begins to decrease following the onset of enhanced precipitation. The ERA-I and OISST data reveal the following relationship between net surface flux and SST: the decreased (increased) LHF/SHF and increased (decreased) downward radiation flux leading (lagging) the positive (negative) SSTA east (west) of anomalous deep convection. This well-known lead–lag relationship reflecting the active air–sea interaction in an MJO is realistically simulated in the coupled experiment C–30NS (not shown).

The contrast between C–30NS and A–CTL confirms the key role of the air–sea interaction in contributing to the eastward propagation and demonstrates that the eastward propagation simulation can be markedly improved by incorporating the air–sea interaction process in the model, even when using a simple 1-D ocean model such as SIT.

3.1.5 Vertically tilting structure

The warm SST was the key forcing that contributed to the boundary layer convergence before the onset of deep convection (Li et al., 2020; Tseng et al., 2014). Hence, the warmer upper ocean enhances the low-level atmospheric convergence and then leads to enhanced low-level moisture and preconditioned deep convection and eastward propagation. This moistening process associated with warm ocean surface temperature is well simulated in the coupled experiment C–30NS but is not shown here. Instead, we present the coupling of moisture divergence (MD) and atmospheric circulation.

MD and zonal wind anomalies from the surface to the upper troposphere averaged over the 10°S–10°N and 120–150°E region are shown in Fig. 4d–f to depict the relationship between the vertically tilting structure of MD and zonal wind anomalies. Note that the active convection occurred around phase 5. The coupled experiment C–30NS (Fig. 4e) realistically simulates the deepening of coupled MD and zonal wind anomalies with time (Fig. 4d). An evolution from the right to left seen in each panel of Fig. 4d–f is equivalent to the eastward movement of vertically tilting circulation from the eastern IO into the MC because of the eastward-propagating nature of the MJO. Figure 4d and 4e show that in both ERA-I reanalysis and the coupled experiment C–30NS, the near-surface convergence (negative MD) occurring in the easterly anomalies lead the convection and continued deepening up to 500 hPa from phase 2 to phase 6 when the easterly anomalies switch to westerly anomalies. By contrast, this evolution of coupled MD–zonal wind anomalies are not appropriately simulated in the uncoupled experiment (Fig. 4f). For example, a slow deepening with time is observed in the MD anomaly but not in the zonal wind anomaly that exhibits a vertically decayed structure, suggesting that MD and wind anomalies are not well coupled, as noted in the ERA-I/NOAA data and the control coupled experiment.

In the ERA-I reanalysis data, the negative near-surface MD anomalies appear first under the easterly anomaly and continue deepening between the easterly and westerly anomalies. This development in the phase relationship between MD and zonal wind anomalies in both ERA-I reanalysis data and the coupled simulation is consistent with the well-known structure embedded in the MJO, namely the near-surface convergence in the easterly phase (i.e., a boundary-layer moistening process; Kiranmayi and Maloney 2011; Li et al., 2020; Tseng et al., 2014), followed by the deep convection when transitioning to the westerly phase. This close phase

relationship that is key to the eastward propagation is appropriately simulated in the coupled experiment but not in the uncoupled experiment.

3.1.6 Intraseasonal variance of precipitation

Figure 4g–i present the spatial distribution of intraseasonal variance of precipitation. In the GPCP data, the maximum variance is noted over the tropical eastern IO, MC, and tropical WP. The maximum variance south of the island in the MC and the equator in the tropical WP reflects the southward shift of the MJO deep convection when passing through the MC, partly due to the blocking effect of mountainous islands and the higher moisture content over high SST south of the equator in the region during boreal winter (Kim et al., 2017; Ling et al., 2019; Sobel et al., 2008; Tseng et al., 2017; Wu and Hsu, 2009). Although the control coupled experiment fails to simulate the variance maximum in the tropical eastern IO, it appropriately simulates the maximum variance over the tropical WP, reflecting its ability to simulate the eastward propagation of the MJO through the MC. By contrast, the uncoupled A–CTL experiment simulates considerably weaker intraseasonal variance in both the tropical eastern IO and the tropical WP. Figure 4j–l are the 20–100-day filtered SST (K, shaded) and 850-hPa wind (m s^{-1}, vector) during MJO phase 7 when deep convection is the strongest over the dateline. The coupled experiment C–30NS realistically simulates the negative SST anomaly over the MC and WP when enhanced tropical convection passed through the MC to the dateline, indicating the capability of the SIT model to reproduce the SST anomaly by exchanging LHF/SHF between the atmosphere and ocean. In A-CTL, no SST anomaly is evident because the model was forced by prescribed climatological SST. The contrast seen in Fig. 4j–l demonstrates the essential role of atmosphere–ocean coupling in shaping the MJO. A delayed air–sea interaction mechanism was noted,

where a preceding active-phase MJO may trigger an inactive-phase MJO through the delayed effect of the induced SST anomaly. In addition, the westerly winds at 850 hPa moving southward between MC and WP are captured by the control experiment C–30NS and are similar to the ERA-I reanalysis winds (Fig. 4j and 4k). By contrast, A–CTL forced by climatological monthly SST (<0.05 K phase^{-1} anomaly) fails to simulate the southward westerly wind of the region extending from the MC to the dateline (Fig. 4l).

3.2 Effect of upper-ocean vertical resolution

In the control coupled experiment C–30NS, the vertical resolution in the upper 10.5 m was 1 m. Tseng et al. (2014) suggested that fine vertical resolution is crucial for appropriately simulating the eastward propagation. To investigate the effect of vertical resolution, two experiments with a thicker first layer were conducted by moving the center of the layer to 11.5 m (C–LR12m) and 33.9 m (C–LR34m), respectively, as opposed to the control experiment in which 10 layers were implemented in the first 10.5 meters (see supplementary Fig. S1 for vertical discretization). The W–FS spectral peaks of U850 in C–LR12m are concentrated in eastward-propagating wavenumber 1 at three timescales (e.g., longer than 80 days, 30–80 days, and approximately 30 days; Fig. 5a). In C–LR34m, both eastward and westward signals are simulated with the dominant W–FS timescale longer than 80 days (Fig. 5b). The appearance of both eastward and westward signals at a lower frequency implied a stronger stationary tendency or weaker eastward-propagating tendency. This result is consistent with that reported by Tseng et al. (2014) that the scientific reproducibility of coarser resolution causes a longer intraseasonal periodicity and slower eastward propagation of the MJO.

The effect of vertical resolution on the MJO simulation can be seen in the

Hovmöller diagram. The eastward propagation simulated in C–LR12m (Fig. 5c) markedly weakened after crossing the MC compare with that simulated in the control experiment C–30NS (Fig. 2e). In C–LR34m, the quasi-stationary fluctuation and westward propagation are simulated over the IO (Fig. 5d), appearing similar to those in A–CTL (Fig. 2f). The lead–lag relationship between precipitation (zonal wind) and SST is poorly simulated in C–LR12m (Fig. 5e) and even more poorly simulated in C–LR34m (Fig. 5f). This result confirms the finding reported by Tseng et al. (2014) that a higher vertical resolution in the upper few meters below the surface allows for a faster air–sea interaction, thus resulting in a more realistic simulation of the MJO.

3.3 Effect of the lowest boundary of the SIT model

The ocean is a vital energy source for the MJO. Although vertical resolution is crucial for the efficiency of air–sea interaction, the thickness of the upper ocean that interacts with the atmosphere represents the ocean heat content to substantiate the MJO. A key question is how thick a vertically-gridded ocean mixed layer should be for a realistic simulation. To explore this issue, three experiments with a model ocean with a 1-m vertical resolution and the ocean model (SIT) bottom at 10, 30, and 60 m, which included the top 12, 14, and 16 levels, respectively, as shown in supplementary Fig. S2 and Table 1, were conducted. The spectra and the Hovmöller diagrams shown in Fig. 6a–c and Fig. 6d–f, respectively, demonstrate that the thicker ocean model simulates a stronger MJO with a frequency closer to those in the coupled experiment C–30NS and ERA-I/NOAA data, and more realistic eastward propagation. In addition, the lead–lag relationship between precipitation (wind) and SST is more realistically simulated with increasing thickness of the ocean model (Fig. 6g–i).

This result suggests that the thickness of the oceanic mixed layer that interacts with the atmosphere strongly affects the frequency of the simulated MJO. A thinner

(thicker) oceanic mixed layer is more quickly (slowly) recharged and discharged through SHF and LHF exchange between the atmosphere and ocean and therefore likely fluctuates at a faster (slower) tempo. The simulated periodicity is therefore affected by the thickness of oceanic mixed layer (or ocean heat content). Although the result suggests 60 m is an appropriate thickness to realistically simulate the periodicity of the MJO, we did not intend to suggest the exact thickness required for a proper simulation because it might depend on the model. The oceanic mixed layer should be adequately thick to contain a certain amount of heat to generate appropriate periodicity. However, the reason for the intraseasonal time scale (i.e., 20-100 days) should be determined in future studies. This finding does not suggest a constant periodicity because periodicity might be affected by the time-varying structure of the atmosphere and ocean in the real world.

3.4 Effects of coupling domains

The MJO is a planetary-scale phenomenon. Given its large-scale circulation, the air–sea interaction affecting the MJO likely occurs in a much larger area than the region near the major convection anomalies. In this section, we discuss the effect of coupling domain on model ability to simulate the eastward propagation speed and periodicity of the MJO. Four experiments considering the coupling in various domains (C–0_30N, C–0_30S, C–30_180E, and C–30E_75W, Fig. 1) were conducted for the purpose. The results are shown in Fig. 7. The C–0_30N that considered the coupling in the tropics between the equator and 30°N simulates the least realistic MJO propagation in terms of W–FS (Fig. 7a), zonal wind–precipitation coupling (Fig. 7e), and SST–precipitation (Fig. 7i) among the four regional coupling experiments. By contrast, coupling only the tropics between the equator and 30°S simulates a more realistic MJO in all three aspects (i.e., spectrum in Fig. 7b, temporal evolution of

500 precipitation/wind, and precipitation/SST coupling in Fig. 7f and 7j). Figure. 8a
501 indicates that the negative OLR anomalies at phase 5 simulated in C–0_30N stays
502 mainly north of the equator and does not shift southward in the MC as revealed in
503 ERA-I reanalysis and NOAA OLR and in the control experiment C–30NS, and the
504 convection over the IO is unrealistically weak. By contrast, the southward detouring
505 in the MC is realistically simulated in C–0_30S that coupled only the tropical ocean
506 between the equator and 30°S. This result indicates that air–sea coupling occurring
507 south of the equator is the key to producing appropriate eastward propagation and
508 detouring of the MJO through the MC. Without this coupling, the C–0_30N
509 experiment fails to realistically simulate the eastward propagation of the MJO (Fig.
510 7e). This contrast can be attributed to the warmer ocean surface and higher moisture
511 content found south of the equator in boreal winter, which comprise a more favorable
512 environmental condition for air–sea coupling and convection–circulation coupling and
513 the occurrence of the MJO.
514 MJO simulations can be affected by air–sea coupling in the longitudinal domain.
515 Tseng et al. (2014) examined this effect by allowing coupling in different regions
516 (e.g., the IO, WP, and IO + WP) and found that the IO + WP coupling experiment
517 yielded the most satisfactory MJO simulation in terms of the zonal W–FS and
518 eastward propagation characteristics. In this study, we conducted sensitivity
519 experiments in which we allowed coupling in the tropics in two longitudinal domains,
520 namely 30°E–180°E (C–30_180E) and 30°E–75°W (C–30E_75W). The 30°E–180°E
521 region covered the IO and WP, and the 30°E–75°W region covered the IO and the
522 entire tropical Pacific. As shown in Fig. 7, the C–30E_75W experiment simulates
523 more realistic MJO than the C–30_180E experiment, with stronger eastward
524 propagation and larger amplitudes in the spectrum (Fig. 7c and 7d) and Hovmöller
525 diagrams of precipitation/wind (Fig. 7g and 7h) and precipitation/SST (Fig. 7k and

7l). The simulated MJO in C–30E_75W propagated farther east than that in C–30_180E, particularly evident in Fig. 7k and 7l. The spatial distributions of circulation and OLR shown in Fig. 8c and 8d indicate the presence of a stronger convective-coupled circulation system over the MC and WP in C–30E_75W. These results suggest that coupling over the entire tropical IO and Pacific could enhance the strength and eastward propagation of the MJO and encourage farther propagation to the central Pacific.

3.5 Diurnal versus no diurnal cycle in air–sea coupling

Previous studies showed that the diurnal cycle in the MC can weaken the MJO and its eastward propagation (Hagos et al., 2016; Oh et al., 2013). We conducted an experiment to determine whether computing surface heat fluxes using daily mean values, instead of instantaneous values, of atmospheric variables and SST with the same coupling frequency would affect the MJO simulation. The coupling in the model was conducted through the SHF and LHF exchange between the atmosphere and ocean, that were calculated based on simulated winds, moisture, and temperature. As mentioned in Section 2.3, air–sea fluxes were calculated twice for every time step (coupling 48 times per day) in the control coupled experiment (C–30NS) based on the instantaneous values of atmospheric and oceanic variables. In the experiment in which the diurnal cycle was removed (C–30NS–nD), air–sea fluxes were calculated as in C–30NS but were based on daily means of both atmospheric variables and SST. Doing this removed certain diurnal effects of air-sea coupling. The results shown in Fig. 9 reveal the enhancement of the eastward-propagating signals in the MJO (e.g., a larger amplitude in spectrum; Fig. 9a) and further eastward propagation (Fig. 9b) as well stronger coupling between precipitation and SST (Fig. 9c) in C–30NS–nD. The overall results are consistent with previous finding that the diurnal cycle tends to

552 reduce the amplitude of the MJO, indicating that the weakening effect occurs through
553 air–sea coupling in addition to those processes in the atmosphere. Previous studies
554 have hypothesized that rapid interaction processes in the diurnal time scale tend to
555 extract energy from the MJO, thus reducing the strength and propagation tendency of
556 the MJO. However, a comparison between the spectra of C–30NS and C–30NS–nD
557 indicates that the experiment in which the diurnal cycle is removed appeared to
558 oversimulate the MJO with unrealistic strength, suggesting that the effect of the
559 diurnal cycle should be considered in the model to simulate a more realistic MJO.
560 However, whether this is a common result in different models remain to be examined.
561
562 **4. Discussion and conclusions**
563 Air–sea coupling is a key mechanism for the successful simulation of the MJO
564 (Chang et al., 2019; DeMott et al., 2015; Jiang et al., 2015, 2020; Kim et al., 2010; Li
565 et al., 2016; Li et al., 2020; Newman et al., 2009; Tseng et al., 2014). This study,
566 following the study of Tseng et al. (2014), demonstrated that coupling a high-
567 resolution 1-D TKE ocean model (namely the SIT model) to the CAM5, namely the
568 CAM5–SIT, significantly improved the MJO simulation over the standalone CAM5.
569 By coupling SIT model to an AGCM different from Tseng et al. (2014), this study
570 confirms the scientific reproducibility for the improvement of MJO simulation in
571 modeling science. The CAM5–SIT realistically simulates the MJO characteristics in
572 many aspects (e.g., intraseasonal periodicity, eastward propagation, coherence in the
573 low-frequency band, detouring propagation across the MC, tilting vertical structure,
574 and intraseasonal variance in the WP).
575 Systematic sensitivity experiments were conducted to investigate the effects of
576 the vertical resolution and the thickness of the 1-D ocean model, coupling domains,
577 and the absence of the diurnal cycle. The results of all the sensitivity experiments are

summarized in Fig. 10a and 10b, which show four common metrics for MJO evaluation. The four metrics are the propagation speed of the MJO (estimated from the U850 Hovmöller diagram as Fig. 2d–f) versus the power ratio of eastward- and westward-propagating 30–80-day signals (E/W ratio, derived from the zonal W–FS) in Fig. 10a and the eastward propagation speed of the 30–80-day filtered precipitation anomaly (estimated from the precipitation Hovmöller diagram) versus the variance explained by RMM1 and RMM2 (i.e., the sum of the variance explained by EOF1 and EOF2 based on Wheeler and Hendon, 2004) in Fig. 10b. Based on the maximum precipitation anomaly and zero values of U850 (indicating deep convection region), propagation speeds of precipitation and U850 were calculated from Hovmöller diagrams between 60°E and 150°W. Overall, the control experiment C–30NS simulates the most realistic MJO among all sensitivity experiments.

As for vertical resolution, we determined that the MJO simulation efficiency decreased when the vertical resolution of the SIT model is decreased from 1 m to 12 or 34 m, as simulated in the C–LR12m and C–LR34m experiments, respectively. This finding, consistent with that reported by Tseng et al. (2014), suggests that a finer vertical resolution more effectively resolves temperature variations in the ocean warm layer and enhances atmospheric–ocean coupling, thus enabling the upper ocean to more efficiently respond to atmospheric forcing by providing sensible and latent heat fluxes; this results in superior synchronization between the lower atmosphere and the upper ocean.

We observed that the shallower ocean model bottom could speed up the eastward propagation of the MJO by producing more perturbations of shorter periodicity (Fig. 6) and results in a weaker MJO. The shallower oceanic mixed layer likely responds more quickly to atmospheric forcing but provides less sensible and latent heat fluxes to the atmosphere. Thus, the MJO propagates too fast with a weaker amplitude.

In the coupling domain sensitivity experiments, we investigated the essential coupling domain required to simulate the realistic MJO and the effect of the domain on the MJO simulation. Coupling only the northern tropics fails to simulate the eastward propagation, whereas coupling only the southern tropics yields a more realistic MJO simulation, although this simulation is inferior to coupling the entire tropics. This contrast reveals the importance of the southern tropical ocean, especially in the MC where high SST and moisture content are noted. Coupling in the southern tropics is therefore essential for providing the energy required to maintain the MJO and its eastward propagation. By contrast, the northern tropics are relatively dry and cool. Coupling in this region is therefore less effective in improving MJO simulation.

In the longitudinal domain sensitivity experiments, we found that the MJO amplitude and the eastward extend of its eastward propagation are enhanced by extending the eastern boundary of the coupling domain from the tropical eastern IO to the tropical WP and further to the tropical eastern Pacific (Fig. 1). Further extension of the domain to cover the tropical Atlantic does not exhibit further enhancement (not shown). This result indicates that coupling in the tropical central and eastern Pacific, although not the major MJO signal regions (i.e., from the tropical IO to the tropical WP), still played a marked role in sustaining the MJO. We propose the following to explain this effect. Because of the planetary scale of the MJO, the near-surface easterly circulation to the east of the convection core often extended to the tropical central and eastern Pacific where the climatological easterly prevailed. The coupling beyond the WP increased low-level moisture transport and convergence to the east of the convection and establish an environment suitable for the further eastward propagation of the MJO. This effect was likely terminated by the landmass of Central America when the tropical Atlantic was further included. Thus, a further eastward extension of the coupling domain exerted little effect on further enhancing the MJO. A

630 diagnostic study on the effect of the longitudinal coupling domain is being conducted,
631 and the results will be reported in a following paper.
632 The diurnal versus nondiurnal cycle experiment indicates that nondiurnal
633 coupling tended to enhance eastward-propagating signals but slow down the eastward
634 propagation (Fig. 10a–b). This result is consistent with the finding of previous studies
635 that the diurnal cycle in the atmosphere extracts energy from the MJO, thus
636 weakening it.
637 In this study, we demonstrated how air–sea coupling can improve the MJO
638 simulation in a GCM. The findings are as follows.
639 (1) Better resolving the fine structure of the upper-ocean temperature and therefore
640 the air–sea interaction leads to more realistic intraseasonal variability in both
641 SST and atmospheric circulation.
642 (2) An adequate thickness of the oceanic mixed layer is required to simulate a delayed
643 response of the upper ocean to atmospheric forcing and lower-frequency
644 fluctuation.
645 (3) Coupling the tropical eastern Pacific, in addition to the tropical IO and the tropical
646 WP, can enhance the MJO and facilitate the further eastward propagation of the
647 MJO to the dateline.
648 (4) Coupling the southern tropical ocean, instead of the norther tropical ocean, is
649 essential for simulating a realistic MJO.
650 (5) Stronger MJO variability can be obtained without considering the diurnal cycle in
651 coupling.
652 Our study confirmed the effectiveness of air–sea coupling for improving MJO
653 simulation in a climate model and demonstrated how and where to couple. The
654 findings enhance our understanding of the physical processes that shape the
655 characteristics of the MJO.

Code and data availability. The model code of CAM5–SIT is available at https://doi.org/10.5281/zenodo.5510795. Input data of CAM5–SIT using the climatological Hadley Centre Sea Ice and Sea Surface Temperature dataset and GODAS data forcing, including 30-year numerical experiments, are available at https://doi.org/10.5281/zenodo.5510795.

Author contributions. HHH is the initiator and the primary investigator of the Taiwan Earth System Model project. YYL is the CAM5–SIT model developer and writes the majority part of the paper. WLT and LCJ assist in MJO analysis.

Competing interests. The authors declare that they have no conflict of interest.

Acknowledgements. The contribution from YYL, HHH, WLT, and LCJ to this study is supported by Ministry of Science and Technology of Taiwan under contracts MOST 110-2123-M-001-003, MOST 110-2811-M-001-603, MOST 109-2811-M-001-624 and MOST108-2811-M-001-643. Our deepest gratitude goes to the editors and anonymous reviewers for their careful work and thoughtful suggestions that have helped improve this paper substantially. We sincerely thank the National Center for Atmospheric Research and their Atmosphere Model Working Group (AMWG) for release CESM1.2.2. We thank the computational support from National Center for High530 performance Computing of Taiwan. This manuscript was edited by Wallace Academic Editing.

Reference

Adler, R. F., Huffman, G. J., Chang, A., Ferraro, R., Xie, P. P., Janowiak, J., Rudolf, B., Schneider, U., Curtis, S., Bolvin,

683 D., Gruber, A., Susskind, J., Arkin, P., and Nelkini, E.: The
684 Version 2.1 Global Precipitation Climatology Project (GPCP)
685 Monthly Precipitation Analysis (1979 -Present), J. Hydrometeor.,
686 4(6), 1147-1167, https://doi.org/10.1175/1525-
687 7541(2003)004<1147:TVGPCP>2.0.CO;2, 2003.

688 Ahn, M.-S., Kim, D., Kang, D., Lee, J., Sperber, K. R., and Glecker, P.
689 J., et al.: MJO propagation across the Maritime Continent: Are
690 CMIP6 models better than CMIP5 models? Geophys. Res. Lett., 47,
691 e2020GL087250, https://doi.org/10.1029/2020GL087250, 2020.

692 Ahn, M.-S., Kim, D., Sperber, K. R., Kang, I.-S., Maloney, E., Waliser,
693 D., and Hendon, H.: MJO simulation in CMIP5 climate models:
694 MJO skill metrics and process-oriented diagnosis, Clim.
695 Dyn., 49, 4023–4045, https://doi.org/10.1007/s00382-017-3558-4,
696 2017.

697 Alappattu, D. P., Wang, Q., Kalogiros, J., Guy, N., and Jorgensen, D.
698 P.: Variability of upper ocean thermohaline structure during a MJO
699 event from DYNAMO aircraft observations, J. Geophys. Res. -
700 Oceans, 122, 1122–1140, https://doi.org/10.1002/2016JC012137,
701 2017.

702 Amante, C., and Eakins, B. W.: ETOPO1 1 arc-minute globe relief
703 model: Procedures, data sources and analysis, NOAA Tech. Memo.
704 NESDIS NGDC-24, 19 pp., NOAA, Silver Spring, Md., 2009.

705 Behringer, D. W., and Xue, Y.: Evaluation of the global ocean data
706 assimilation system at NCEP: The Pacific Ocean. Eighth
707 Symposium on Integrated Observing and Assimilation Systems for
708 Atmosphere, Oceans, and Land Surface, AMS 84th Annual
709 Meeting, Washington State Convention and Trade Center, Seattle,
710 Washington, 11-15. Derber, J.C., and A. Rosati, 1989: A global
711 oceanic data assimilation system, J. Phys. Oceanogr., 19, 1333–
712 1347, https://ams.confex.com/ams/pdfpapers/70720.pdf, 2004.

713 Bentsen, M., Bethke, I., Debernard, J. B., Iversen, T., Kirkevåg, A.,
714 Seland, Ø., Drange, H., Roelandt, C., Seierstad, I. A., Hoose, C.,
715 and Kristjánsson, J. E.: The Norwegian Earth System Model,
716 NorESM1-M – Part 1: Description and basic evaluation of the
717 physical climate, Geosci. Model Dev., 6, 687–720,
718 https://doi.org/10.5194/gmd-6-687-2013, 2013.

719 Bernie, D., Guilyardi, E., Madec, G., Slingo, J., Woolnough, S., and
720 Cole, J.: Impact of resolving the diurnal cycle in an ocean–
721 atmosphere GCM. Part 2: a diurnally coupled CGCM, Clim.
722 Dynam., 31, 909–925, https://doi.org/10.1007/s00382-008-0429-z,
723 2008.

724 Boyle, J. S., Klein, S. A., Lucas, D. D., Ma, H.-Y., Tannahill, J., and
725 Xie, S.: The parametric sensitivity of CAM5's MJO, J. Geophys.
726 Res.-Atmos., 120, 1424–1444,
727 https://doi.org/10.1002/2014JD022507, 2015.

728 Bui, H. X., and Maloney, E. D.: Changes in Madden-Julian Oscillation
729 precipitation and wind variance under global warming, Geophys.
730 Res. Lett., 45, 7148–7155, https://doi.org/10.1029/2018GL078504,
731 2018.

732 Chang, M.-Y., Li, T., Lin, P.-L., and Chang, T.-H.: Forecasts of MJO
733 Events during DYNAMO with a Coupled Atmosphere-Ocean
734 Model: Sensitivity to Cumulus Parameterization Scheme, J.
735 Meteorol. Res., 33, 1016–1030, https://doi.org/10.1007/s13351-
736 019-9062-5, 2019.

737 CLIVAR MADDEN–JULIAN OSCILLATION WORKING GROUP:
738 MJO simulation diagnostics, J. Climate, 22, 3006–3030,
739 https://doi.org/10.1175/2008JCLI2731.1, 2009.

740 Crueger, T., Stevens, B., and Brokopf, R.: The Madden–Julian
741 Oscillation in ECHAM6 and the introduction of an objective MJO
742 metric, J. Climate, 26, 3241–3257, https://doi.org/10.1175/JCLI-D-
743 12-00413.1, 2013.

744 Danabasoglu, G., Lamarque, J.-F., Bacmeister, J., Bailey, D. A.,
745 DuVivier, A. K., and Edwards, J., et al.: The Community Earth
746 System Model Version 2 (CESM2), J. Adv. Model. Earth Syst., 12,
747 e2019MS001916, https://doi.org/10.1029/2019MS001916, 2020.

748 Dee, D. P., Uppala, S. M., Simmons, A. J., Berrisford, P., Poli, P.,
749 Kobayashi, S., Andrae, U., Balmaseda, M. A., Balsamo, G., Bauer,
750 P., Bechtold, P., Beljaars, A. C. M., van de Berg, L., Bidlot, J.,
751 Bormann, N., Delsol, C., Dragani, R., Fuentes, M., Geer, A. J.,
752 Haimberger, L., Healy, S. B., Hersbach, H., Hólm, E. V., Isaksen,
753 L., Kållberg, P., Köhler, M., Matricardi, M., McNally, A. P.,
754 Monge-Sanz, B. M., Morcrette, J.-J., Park, B.-K., Peubey, C., de
755 Rosnay, P., Tavolato, C., Thépaut, J.-N., and Vitart, F.: The ERA-
756 Interim reanalysis: configuration and performance of the data
757 assimilation system, Q. J. R. Meteorol. Soc., 137: 553–597,
758 https://doi.org/10.1002/qj.828, 2011.

759 de Szoeke, S. P., Skyllingstad, E. D., Zuidema, P., and Chandra, A.
760 S.: Cold pools and their influence on the tropical marine boundary
761 layer, J. Atmos. Sci., 74, 1149–1168. https://doi.org/10.1175/JAS-
762 D-16-0264.1, 2017.

763 Delworth, T. L., et al.: GFDL's CM2 global coupled climate models.
764 Part 1: Formulation and simulation characteristics, J. Climate, 19,
765 643–674, https://doi.org/10.1175/JCLI3629.1, 2006.

766 DeMott, C. A., Klingaman, N. P., and Woolnough, S. J.: Atmosphere-
767 ocean coupled processes in the Madden-Julian oscillation, Rev.
768 Geophys., 53, 1099–1154, https://doi.org/10.1002/2014RG000478,
769 2015.

770 DeMott, C. A., Klingaman, N. P., Tseng, W.-L., Burt, M. A., Gao, Y.,
771 and Randall, D. A.: The convection connection: How ocean

feedbacks affect tropical mean moisture and MJO propagation, J. Geophys. Res.-Atmos., 124, 11,910–11,931, https://doi.org/10.1029/2019JD031015, 2019.

Haertel, P.: Prospects for Erratic and Intensifying Madden-Julian Oscillations, Climate, 8, 24, https://doi.org/10.3390/cli8020024, 2020.

Hannah, W. M., and Maloney, E. D.: The moist static energy budget in NCAR CAM5 hindcasts during DYNAMO, J. Adv. Model. Earth Syst., 6, 420–440, https://doi.org/10.1002/2013MS000272, 2014.

Hagos, S. M., Zhang, C., Feng, Z., Burleyson, C. D., Mott, C. De, Kerns, B., Benedict, J. J., and Martini, M. N.: The impact of the diurnal cycle on the propagation of Madden-Julian Oscillation convection across the Maritime Continent, J. Adv. Model. Earth Syst., 8, 1552–1564, https://doi.org/10.1002/2016MS000725, 2016.

He, S., Yang, S., and Li, Z.: Influence of Latent Heating over the Asian and Western Pacific Monsoon Region on Sahel Summer Rainfall, Sci. Rep. 7, 7680, https://doi.org/10.1038/s41598-017-07971-6, 2017.

Heath, A., Gonzalez, A. O., Gehne, M., and Jaramillo, A.: Interactions of large-scale dynamics and Madden-Julian Oscillation propagation in multi-model simulations, J. Geophys. Res.-Atmos., 126, e2020JD033988. https://doi.org/10.1029/2020JD033988, 2021.

Hong, X., Reynolds, C. A., Doyle, J. D., May, P., and O'Neill, L.: Assessment of upper-ocean variability and the Madden-Julian Oscillation in extended-range air–ocean coupled mesoscale simulations, Dyn. Atmos. Oceans, 78, 89–105. https://doi.org/10.1016/j.dynatmoce.2017.03.002, 2017.

Hung, M.-P., Lin, J.-L., Wang, W., Kim, D., Shinoda, T., and Weaver, S. J.: MJO and convectively coupled equatorial waves simulated by CMIP5 climate models, J. Climate, 26, 6185–6214, https://doi.org/10.1175/JCLI-D-12-00541.1, 2013.

Hurrell, J. W., Holland, M. M., Gent, P. R., Ghan, S., Kay, J. E., Kushner, P. J., Lamarque, J.-F., Large, W. G., Lawrence, D., Lindsay, K., Lipscomb, W. H., Long, M. C., Mahowald, N., Marsh, D. R., Neale, R. B., Rasch, P., Vavrus, S., Vertenstein, M., Bader, D., Collins, W. D., Hack, J. J., Kiehl, J., and Marshall, S.: The community Earth system model: A framework for collaborative research, B. Am. Meteorol. Soc., 94, 1319–1360, https://doi.org/10.1175/BAMS-D-12-00121, 2013.

Jiang, X., et al.: Vertical structure and physical processes of the MaddenJulian oscillation: Exploring key model physics in climate simulations, J. Geophys. Res.-Atmos., 120, 4718–4748, https://doi.org/10.1002/2014JD022375, 2015.

Jiang, X., Adames, Á. F., Kim, D., Maloney, E. D., Lin, H., and Kim,

H., et al.: Fifty years of research on the Madden-Julian Oscillation: Recent progress, challenges, and perspectives, J. Geophys. Res.-Atmos., 125, e2019JD030911, https://doi.org/10.1029/2019JD030911, 2020.

Johnson, R. H., and Ciesielski, P. E.: Multiscale variability of the atmospheric boundary layer during DYNAMO, J. Atmos. Sci., 74, 4003–4021, https://doi.org/10.1175/JAS-D-17-0182.1, 2017.

Kaylor, R. E.: Filtering and decimation of digital time series, Tech. Rep. Note BN 850, Institute for Physical Science and Technology, University of Maryland at College Park, 14 pp., 1977.

Kim, D., Sobel, A. H., Maloney, E. D., Frierson, D. M., and Kang, I.-S.: A systematic relationship between intraseasonal variability and mean state bias in AGCM simulations, J. Climate, 24, 5506–5520. https://doi.org/10.1175/2011JCLI4177.1, 2011.

Kim, D., Kim H., and Lee, M.-I.: Why does the MJO detour the Maritime Continent during austral summer? Geophys. Res. Lett., 44, 2579–2587, https://doi.org/10.1002/2017GL072643, 2017.

Kim, H.-M., Hoyos, C. D., and Webster, P. J. et al.: Ocean–atmosphere coupling and the boreal winter MJO, Clim Dynam., 35, 771–784, https://doi.org/10.1007/s00382-009-0612-x, 2010.

Kiranmayi, L., and Maloney, E. D.: Intraseasonal moist static energy budget in reanalysis data, J. Geophys. Res., 116, D21117, https://doi.org/10.1029/2011JD016031, 2011.

Lan, Y.-Y., Tsuang, B.-J., Tu, C.-Y., Wu, T.-Y., Chen, Y.-L., and Hsieh, C.-I.: Observation and Simulation of Meteorology and Surface Energy Components over the South China Sea in Summers of 2004 and 2006, Terr. Atmos. Ocean. Sci., 21, 325–342, https://doi.org/ 10.3319/TAO.2009.04.07.01(A), 2010.

Lee, H.-T., and NOAA CDR Program: NOAA Climate Data Record (CDR) of Daily Outgoing Longwave Radiation (OLR), Version 1.2, NOAA National Climatic Data Center, https://doi.org/10.7289/V5SJ1HH2, 2011.

Li, T., Ling, J., and Hsu, P.-C.: Madden–Julian Oscillation: Its discovery, dynamics, and impact on East Asia, J. Meteor. Res., 34, 20–42, https://doi.org/10.1007/s13351-020-9153-3, 2020.

Li, T., Tam, F., Fu, X., Zhou, T., and Zhu, W.: Causes of the intraseasonal SST variability in the tropical Indian Ocean, Atmos. Oceanic Sci. Lett., 1, 18–23, https://doi.org/10.1080/16742834.2008.11446758, 2008.

Li, X., Tang, Y., Zhou, L., Chen, D., and Yao, Z.: Assessment of Madden–Julian oscillation simulations with various configurations of CESM, Clim. Dynam., 47, 2667–2690, https://doi.org/10.1007/s00382-016-2991-0, 2016.

865 Ling, J., Zhao, Y., and Chen, G.: Barrier effect on MJO propagation by
866 the Maritime Continent in the MJO Task Force/GEWEX
867 atmospheric system study models, J. Climate, 32, 5529–
868 5547, https://doi.org/10.1175/JCLI-D-18-0870.1, 2019.

869 Madden, R. A., and Julian, P. R.: Description of global-scale
870 circulation cells in the tropics with a 40-50 day period, J. Atmos.
871 Sci., 29, 1109-1123, https://doi.org/10.1175/1520-
872 0469(1972)029<1109:DOGSCC>2.0.CO;2, 1972.

873 Madden, R. A., and Julian, P. R.: Observations of the 40-50 day
874 tropical oscillation - A review, Mon. Weather Rev., 122, 814– 837,
875 https://doi.org/10.1175/1520-
876 0493(1994)122<0814:OOTDTO>2.0.CO;2, 1994.

877 Neale, R. B., et al.,: Description of the NCAR Community Atmosphere
878 Model (CAM 5.0), NCAR Tech. Note NCAR/TN-486+STR, 289
879 pp., Natl. Cent. for Atmos. Res, Boulder, Colo., 2012.

880 Newman, M., Sardeshmukh, P. D., and Penland, C.: How important is
881 air–sea coupling in ENSO and MJO evolution? J.
882 Clim., 22, 2958– 2977, https://doi.org/10.1175/2008JCLI2659.1,
883 2009.

884 Oh, J., Kim, B., and Kim, K. et al.: The impact of the diurnal cycle on
885 the MJO over the Maritime Continent: a modeling study
886 assimilating TRMM rain rate into global analysis, Clim.
887 Dynam., 40, 893–911, https://doi.org/10.1007/s00382-012-1419-8,
888 2013.

889 Pei, S., Shinoda, T., Soloviev, A., and Lien, R.-C.: Upper ocean
890 response to the atmospheric cold pools associated with the
891 Madden-Julian Oscillation, Geophys. Res. Lett., 45, 5020–5029,
892 https://doi.org/10.1029/2018GL077825, 2018.

893 Pujiana, K., Moum, J. N., and Smyth, W. D.: The role of subsurface
894 turbulence in redistributing upper-ocean heat, freshwater, and
895 momentum in response to the MJO in the equatorial Indian
896 Ocean, J. Phys. Oceanogr., 48, 197–
897 220, https://doi.org/10.1175/JPO-D-17-0146.1, 2018.

898 Rayner, N. A., Parker, D. E., Horton, E. B., Folland, C. K., Alexander,
899 L. V., Rowell, D. P., Kent, E. C., and Kaplan, A.: Global analyses
900 of sea surface temperature, sea ice, and night marine air
901 temperature since the late nineteenth century, J. Geophys. Res.,
902 108(D14), 4407, https://doi.org/10.1029/2002JD002670, 2003.

903 Ren, P. F., Gao, L., and Ren, H.-L. et al.: Representation of the
904 Madden–Julian Oscillation in CAMSCSM, J. Meteor. Res., 33,
905 627–650, https://doi.org/10.1007/s13351-019-8118-x, 2019.

906 Reynolds, R. W., and Smith, T. M.: A high-resolution global sea
907 surface temperature climatology, J. Clim., 8(6),1571–1583,
908 https://doi.org/10.1175/1520-

909 0442(1995)008<1571:AHRGSS>2.0.CO;2, 1995.

910 Schreck, C. J., Lee, H.-T., and Knapp, K. R.: HIRS outgoing longwave
911 radiation—Daily climate data record: Application toward
912 identifying tropical subseasonal variability, Remote Sens., 10,
913 1325. https://doi.org/10.3390/rs10091325, 2018.

914 Sobel, A. H., Maloney, E. D., Bellon, G., and Dargan, M. F.: The role
915 of surface heat fluxes in tropical intraseasonal oscillations, Nat.
916 Geosci., 1, 653–657, https://doi.org/10.1038/ngeo312, 2008.

917 Subramanian, A. C., Jochum, M., Miller, A. J., Murtugudde, R., Neale,
918 R. B., and Waliser, D. E.: The Madden–Julian oscillation in
919 CCSM4, J. Climate, 24, 6261–6282, https://doi.org/10.1175/JCLI-
920 D-11-00031.1, 2011.

921 Tseng, W.-L., Tsuang, B.-J., Keenlyside, N. S., Hsu, H.-H. and Tu, C.-
922 Y.: Resolving the upper-ocean warm layer improves the simulation
923 of the Madden-Julian oscillation, Clim. Dynam., 44, 1487–1503,
924 https://doi.org/10.1007/s00382-014-2315-1, 2014.

925 Tseng, W.-L., Hsu, H.-H., Keenlyside, N., Chang, C.-W. J., Tsuang,
926 B.-J., Tu, C.-Y., and Jiang, L.-C.: Effects of Orography and Land–
927 Sea Contrast on the Madden–Julian Oscillation in the Maritime
928 Continent: A Numerical Study Using ECHAM-SIT, J. Climate, 30,
929 9725–9741, https://doi.org/10.1175/JCLI-D-17-0051.1, 2017.

930 Tu, C.-Y., and Tsuang, B.-J.: Cool-skin simulation by a one-column
931 ocean model, Geophys. Res. Lett., 32, L22602,
932 https://doi.org/10.1029/2005GL024252, 2005.

933 Wang, W., Saha, S., Pan, H.-L., Nadiga, S., and White, G.: Simulation
934 of ENSO in the new NCEP Coupled Forecast System Model
935 (CFS03), Mon. Wea. Rev., 133, 1574–1593,
936 https://doi.org/10.1175/MWR2936.1, 2005.

937 Wang, W., Hung, M.-P., Weaver, S. J., Kumar, A., and Fu, X.: MJO
938 prediction in the NCEP Climate Forecast System version 2, Clim.
939 Dyn., 42, 2509–2520, https://doi.org/10.1007/s00382-013-1806-9,
940 2014.

941 Wheeler, M. C., and Hendon, H. H.: An all-season real-time
942 multivariate MJO index: development of an index for monitoring
943 and prediction, Mon. Weather Rev., 132, 1917–1932,
944 https://doi.org/10.1175/1520-
945 0493(2004)132<1917:AARMMI>2.0.CO;2, 2004.

946 Wheeler, M., and Kiladis, G. N.: Convectively coupled equatorial
947 waves: Analysis of clouds and temperature in the wavenumber-
948 frequency domain, J. Atmos. Sci., 56, 374– 399,
949 https://doi.org/10.1175/1520-
950 0469(1999)056<0374:CCEWAO>2.0.CO;2, 1999.

951 Woolnough, S. J., Vitard, F., and Balmaseda, M. A.: The role of the

ocean in the Madden–Julian oscillation: Implications for MJO prediction, Quart. J. Roy. Meteor. Soc., 133, 117–128, https://doi.org/10.1002/qj.4, 2007.

Wu, C.-H., and Hsu, H.-H.: Potential Influence of Topography on the MJO in the Maritime Continent, J. Climate, 22, 5433–5448, https://doi.org/10.1175/2009JCLI2825.1, 2009.

Yoneyama, K., Zhang, C., and Long, C.: Tracking pulses of the Madden–Julian oscillation, Bull. Amer. Meteor. Soc., 94, 1871–1891, https://doi.org/10.1175/BAMS-D-12-00157.1, 2013.

Zhang, C.: Madden-Julian oscillation, Rev. Geophys., 43, RG2003, https://doi.org/10.1029/2004RG000158, 2005.

Zhang, C., and Yoneyama, K.: CINDY/DYNAMO field campaign: Advancing our understanding of MJO initiation, In World Scientific Series on Asia-Pacific Weather and Climate (pp. 339-348). (World Scientific Series on Asia-Pacific Weather and Climate; Vol. Volume 9), World Scientific Publishing Co. Pte Ltd. https://doi.org/10.1142/9789813200913_0027, 2017.

969 Table 1. List of experiments

Section	Category	Experiments	Description
3.1	Coupled or uncoupled	A–CTL	Standalone CAM5.3 forced by forced by the monthly mean Hadley Centre SST dataset version 1 climatology
		C–30NS (the control coupled experiment)	CAM5.3 coupled with SIT over the tropical domain (30°N–30°S), with 41 layers of finest vertical resolution (up to the seabed) and diurnal cycle; the frequency of CAM5 being exchanged with CPL is 48 times per day
3.2	Upper-ocean vertical resolution	C–LR12m	The first ocean vertical level starts at 11.5 m with 31 layers (beside SST and cool skin layer are 11.5 m, 29.5 m and 43.6 m up to the seabed)
		C–LR34m	The first ocean vertical level starts at 33.9 m with 28 layers (beside SST and cool skin layer are 33.9 m, 76.9 m and 96.8 m up to the seabed)
3.3	Lowest boundary of SIT	C–HR1mB10m	The lowest boundary of SIT has a depth of 10 m (model depth between 0 m and 10 m)
		C–HR1mB30m	The lowest boundary of SIT has a depth of 30 m (model depth between 0 m and 30 m)
		C–HR1mB60m	The lowest boundary of SIT has a depth of 60 m (model depth between 0 m and 60 m)
3.4	Regional coupling domain in latitude	C–0_30N	Coupled in the tropical northern hemisphere (0°N–30°N, 0°E–360°E)
		C–0_30S	Coupled in the tropical southern hemisphere (0°S–30°S, 0°E–360°E)
	Regional coupling domain in longitude	C–30_180E	Coupled in the Indo-Pacific (30°N–30°S, 30°E–180°E)
		C–30E_75W	Coupled over the Indian Ocean and Pacific Ocean (30°N–30°S, 30°E–75°W)
3.5	Absence of the diurnal cycle	C–30NS–nD	Absence of the diurnal cycle in C–30NS; the CAM5.3 daily atmospheric mean of surface wind, temperature, total precipitation, net surface heat flux, u-stress and v-stress over water trigger the SIT and daily mean SST feedback to atmosphere; the frequency of CAM5 is exchanged with CPL 48 times per day

970 Experiment abbreviations: “A” means standalone AGCM simulation. “C” means the
971 CAM5.3 coupled to the SIT model.

Figure List

Figure 1. Schematics of coupled and uncoupled domains in the regional coupling experiment: (a) C–30NS, (b) C–0_30N, (c) C–0_30S, (d) C–30_180E, and (e) C–30E_75W. The background is the climatological mean SST in December–February (DJF).

Figure 2. (a)–(c) Zonal wavenumber–frequency spectra for 850-hPa zonal wind averaged over 10°S–10°N in boreal winter after removing the climatological mean seasonal cycle. Vertical dashed lines represent periods at 80 and 30 days, respectively. (d)–(f) Hovmöller diagrams of the correlation between the precipitation averaged over 10°S–5°N, 75–100°E and the intraseasonally filtered precipitation (color) and 850-hPa zonal wind (contour) averaged over 10°N–10°S. (g)–(i) Zonal wavenumber–frequency power spectra of anomalous OLR (colors) and phase lag with U850 (vectors) for the symmetric component of tropical waves, with the vertically upward vector representing a phase lag of 0° with phase lag increasing clockwise. Three dispersion straight lines with increasing slopes represent the equatorial Kelvin waves (derived from the shallow water equations) corresponding to three equivalent depths, 12, 25, and 50 m, respectively. (j)–(l) Composites of 20–100-day filtered OLR (W m^{-2}, shaded) and 850-hPa wind (m s^{-1}, vector) for MJO phase 5 when deep convection is the strongest over the MC and 850-hPa wind, with the reference vector (1 m s^{-1}) shown at the top right of each panel, and (m)–(o) 15°N–15°S averaged p-vertical velocity anomaly (Pa s^{-1}, shaded) and moist static energy anomaly (W m^{-2}, contour, interval 0.003); solid, dashed, and thick-black lines represent positive, negative, and zero values, respectively. The number of days used to generate the composite is shown at the bottom right corner of each panel. (a), (d), (g), (j), and (m) are from the ERA-Interim and NOAA post-processed data (abbr. ERA-I/NOAA); (b), (e), (h), (k), and (n) are from the control experiment C–30NS; and (c), (f), (i), (l), and (o) are from the A–CTL.

Figure 3. Evolution of the filtered OLR anomaly (W m^{-2}, shaded) and 850-hPa wind (m s^{-1}, vector) at phase 2, 4, 6, and 8: (a) the ERA-I/NOAA data, (b) the control coupled experiment C–30NS, and (c) the uncoupled experiment A–CTL. The unit of the reference vector shown at the top right corner of each panel is m s^{-1}, and the number of days used for the composite is shown at the bottom right corner of each panel.

Figure 4. (a)–(c) Phase-longitude Hovmöller diagrams of 20–100-day filtered precipitation (mm day^{-1}, shaded) and SST anomaly (K, contour) averaged over 10°N–10°S from phase 1 to 8. Contour interval is 0.03; solid, dashed, and thick-black lines represent positive, negative, and zero values, respectively. (d)–(f) Phase-vertical Hovmöller diagrams of 20–100-day moisture divergence (shading, 10^{-6} g kg^{-1} s^{-1}) and

zonal wind (contoured, m s^{-1}) averaged over 10°N–10°S, 120–150°E; solid, dashed, and thick-black curves are positive, negative, and zero values, respectively. (g)–(i) Variation of 30–60-day filtered precipitation in the eastern IO and the WP in observation (color shading), and the ratio between intraseasonal and total variance (contoured) and (j)–(l) composites 20–100-day filtered SST (K, shaded) and 850-hPa winds (m s^{-1}, vector) at phase 7 when deep convection was the strongest over the dateline. Reference vector shown at the top right corner of each panel. (a), (d), (g), and (j) are from the ERA-I/NOAA data; (b), (e), (h), and (k) are from the control coupled experiment C–30NS; and (c), (f), (i), and (l) are from the uncoupled experiment A–CTL.

Figure 5. (a)–(b) Same as in Fig. 2(a) but for the C–LR12m and C–LR34m. (c)–(d) Same as in Fig. 2(d) but for the C–LR12m and C–LR34m. (e)–(f) Same as in Fig. 4(a) but for the C–LR12m and C–LR34m.

Figure 6. Same as in Fig. 5 but for the C–HR1mB10m, C–HR1mB30m, and C–HR1mB60m.

Figure 7. Same as in Fig. 5 but for the C–0_30N, C–0_30S, C–30_180E, and C–30E_75W.

Figure 8. Same as in Fig. 3 but for phase 5 in the C–0_30N, C–0_30S, C–30_180E, and C–30E_75W.

Figure 9. Similar as in Fig. 5 but for the C–30NS–nD.

Figure 10. Scattered plots of various MJO indices in the ERA-I/NOAA data and 12 experiments: (a) power ratio of east/west propagating waves of wavenumber 1–3 of 850-hPa zonal winds (X-axis) with a 30–80-day period and eastward propagation speed of U850 anomaly (Y-axis) from the Hovmöller diagram and (b) RMM1 and RMM2 variance and eastward propagation speed of the filtered precipitation anomaly derived from the Hovmöller diagram.

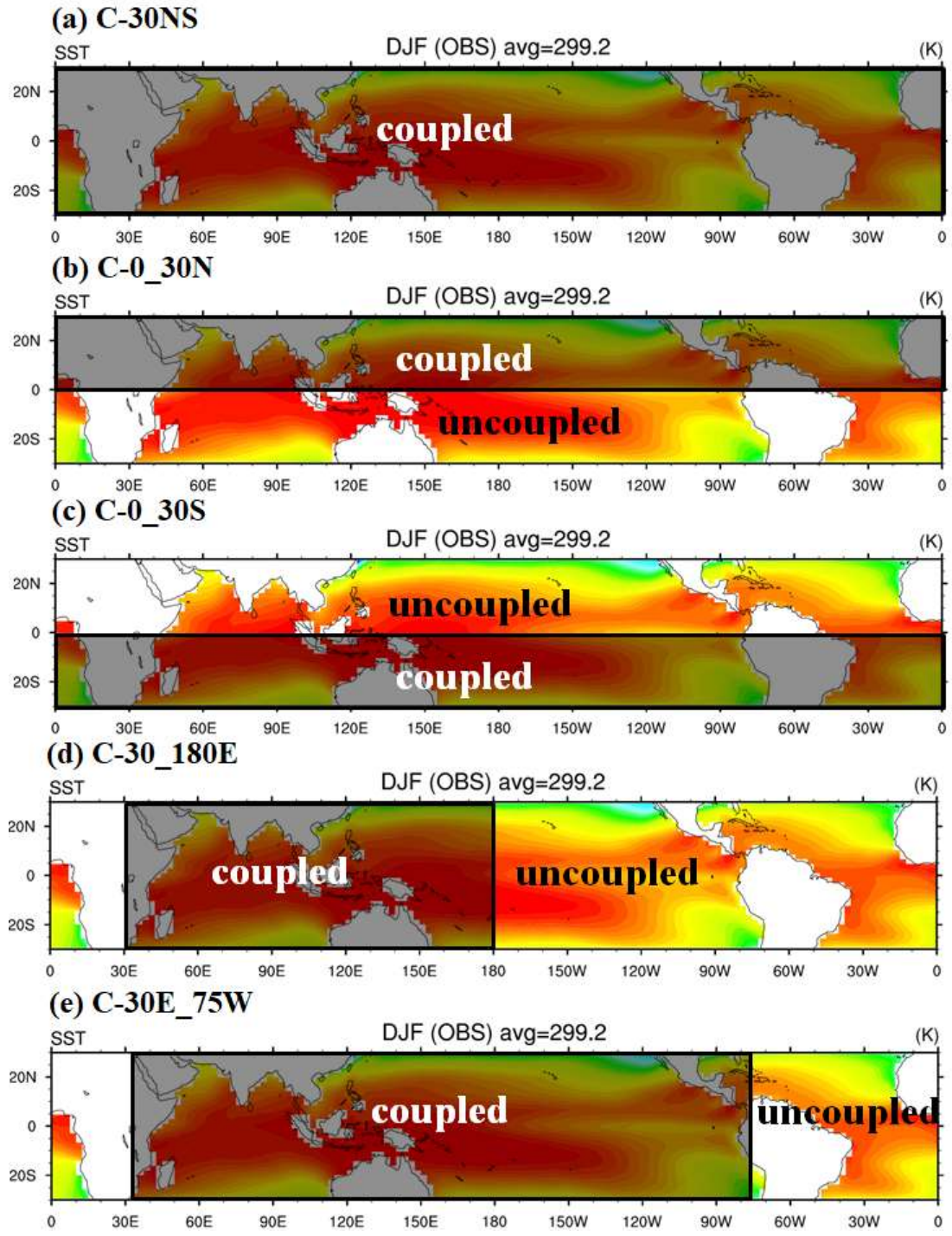

Figure 1. Schematics of coupled and uncoupled domains in the regional coupling experiment: (a) C–30NS, (b) C–0_30N, (c) C–0_30S, (d) C–30_180E, and (e) C–30E_75W. The background is the climatological mean SST in December–February (DJF).

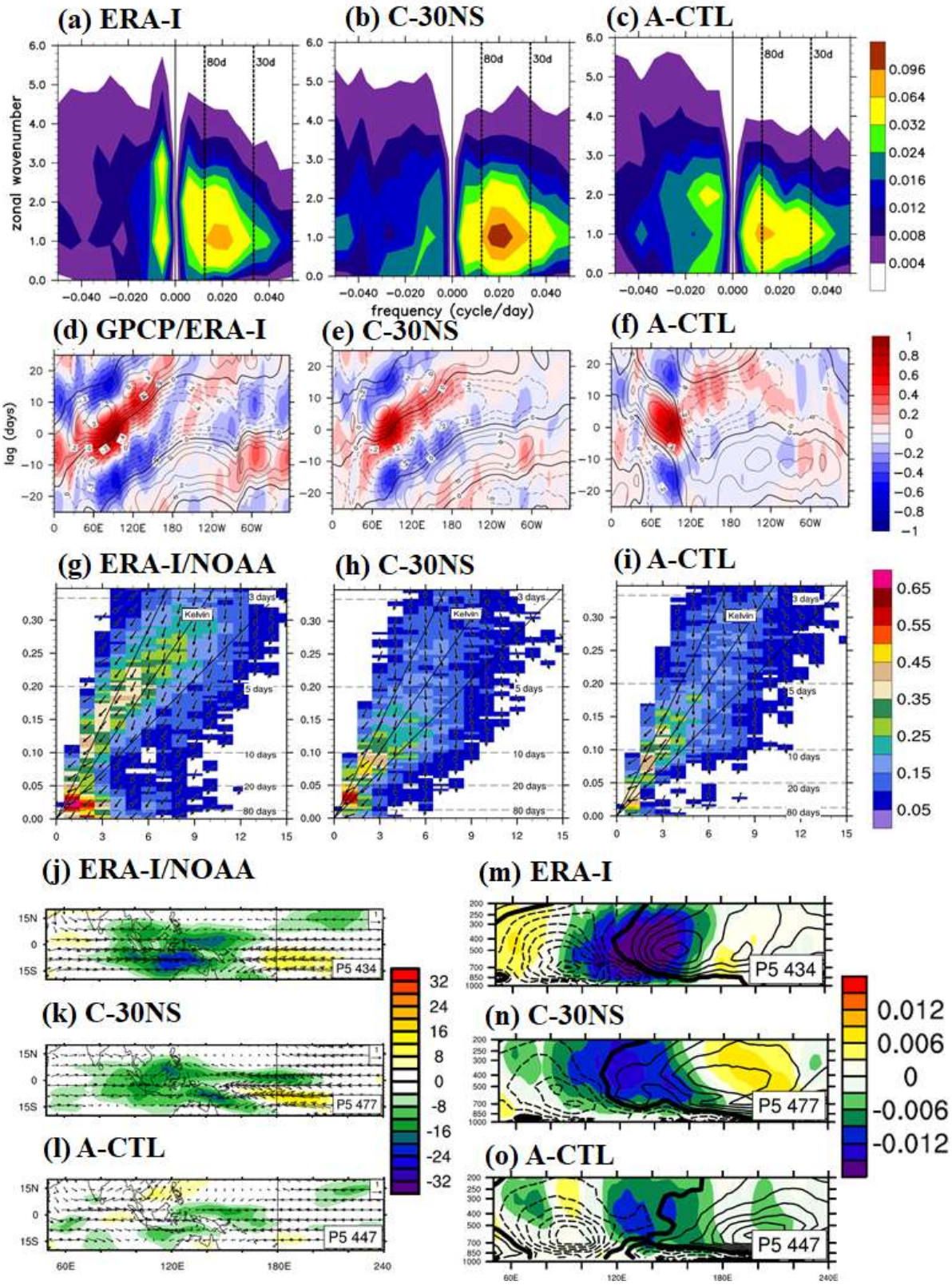

Figure 2. (a)–(c) Zonal wavenumber–frequency spectra for 850-hPa zonal wind averaged over 10°S–10°N in boreal winter after removing the climatological mean seasonal cycle.

Vertical dashed lines represent periods at 80 and 30 days, respectively. (d)–(f) Hovmöller diagrams of the correlation between the precipitation averaged over 10°S–5°N, 75–100°E and the intraseasonally filtered precipitation (color) and 850-hPa zonal wind (contour) averaged over 10°N–10°S. (g)–(i) Zonal wavenumber–frequency power spectra of anomalous OLR (colors) and phase lag with U850 (vectors) for the symmetric component of tropical waves, with the vertically upward vector representing a phase lag of 0° with phase lag increasing clockwise. Three dispersion straight lines with increasing slopes represent the equatorial Kelvin waves (derived from the shallow water equations) corresponding to three equivalent depths, 12, 25, and 50 m, respectively. (j)–(l) Composites of 20–100-day filtered OLR (W m^{-2}, shaded) and 850-hPa wind (m s^{-1}, vector) for MJO phase 5 when deep convection is the strongest over the MC and 850 hPa wind, with the reference vector (1 m s^{-1}) shown at the top right of each panel, and (m)–(o) 15°N–15°S averaged p-vertical velocity anomaly (Pa s^{-1}, shaded) and moist static energy anomaly (W m^{-2}, contour, interval 0.003); solid, dashed, and thick-black lines represent positive, negative, and zero values, respectively. The number of days used to generate the composite is shown at the bottom right corner of each panel. (a), (d), (g), (j), and (m) are from the ERA-Interim and NOAA post-processed data (abbr. ERA-I/NOAA); (b), (e), (h), (k), and (n) are from the control experiment C–30NS; and (c), (f), (i), (l), and (o) are from the A–CTL.

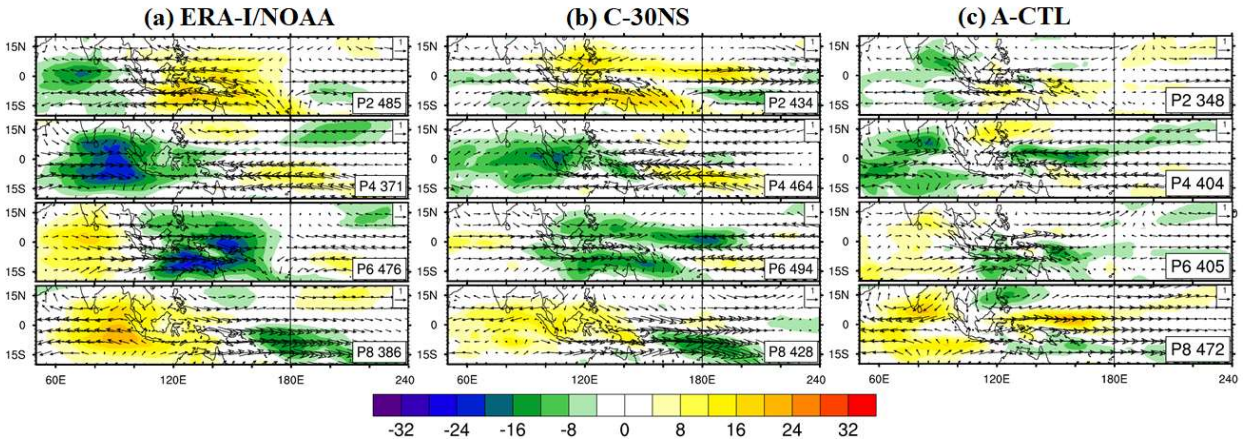

Figure 3. Evolution of the filtered OLR anomaly (W m^{-2}, shaded) and 850-hPa wind (m s^{-1}, vector) at phase 2, 4, 6, and 8: (a) the ERA-I/NOAA data, (b) the control coupled experiment C–30NS, and (c) the uncoupled experiment A–CTL. The unit of the reference vector shown at the top right corner of each panel is m s^{-1}, and the number of days used for the composite is shown at the bottom right corner of each panel.

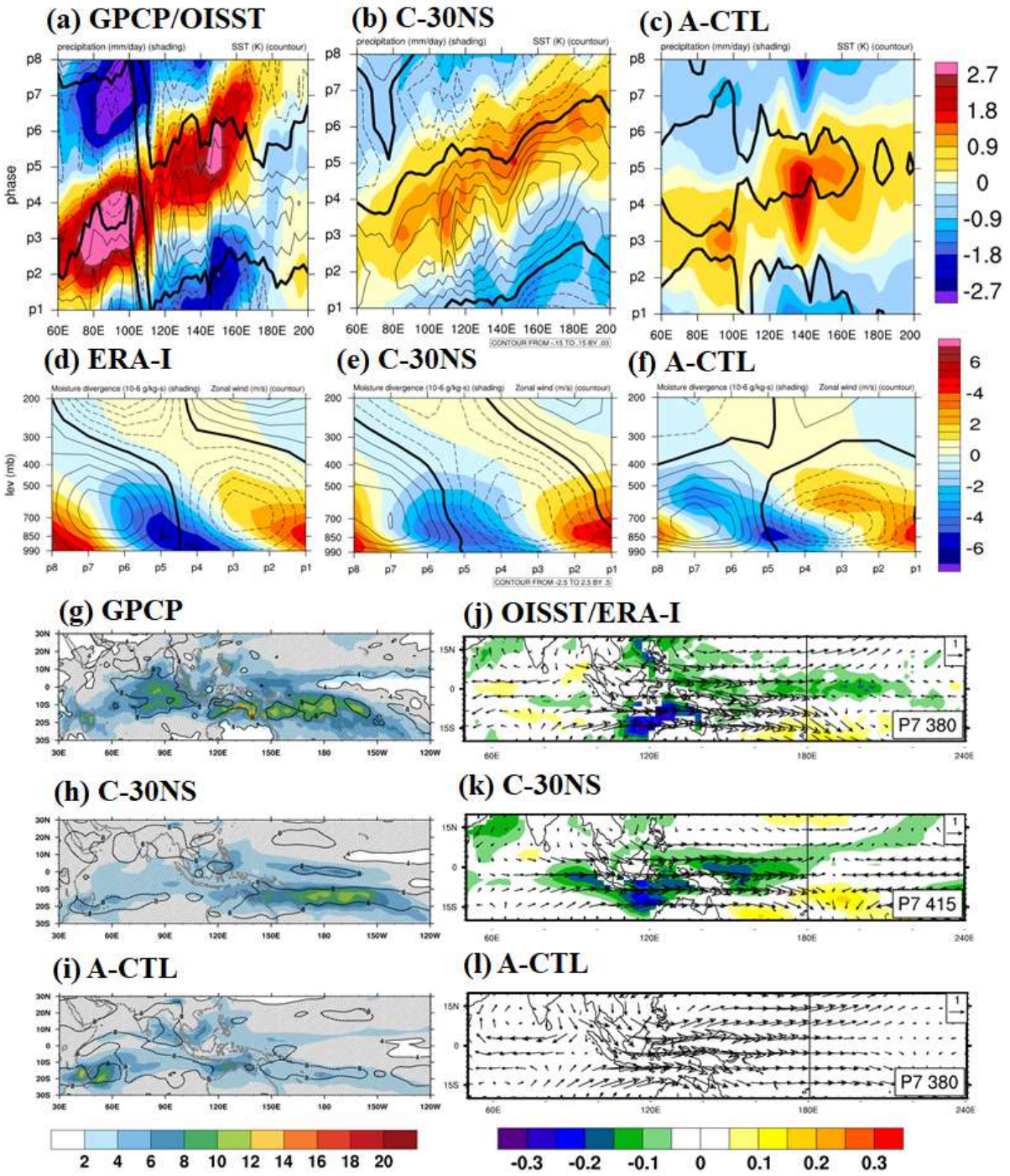

Figure 4. (a)–(c) Phase-longitude Hovmöller diagrams of 20–100-day filtered precipitation (mm day^{-1}, shaded) and SST anomaly (K, contour) averaged over 10°N–10°S from phase 1 to 8. Contour interval is 0.03; solid, dashed, and thick-black lines represent positive, negative, and zero values, respectively. (d)–(f) Phase-vertical Hovmöller diagrams of 20–100-day moisture divergence (shading, 10^{-6} g kg^{-1} s^{-1}) and zonal wind (contoured, m s^{-1}) averaged over 10°N–10°S, 120–150°E; solid, dashed, and thick-black curves are positive, negative, and zero values, respectively. (g)–(i) Variation

of 30–60-day filtered precipitation in the eastern IO and the WP in observation (color shading), and the ratio between intraseasonal and total variance (contoured) and (j)–(l) composites 20–100-day filtered SST (K, shaded) and 850-hPa winds (m s^{-1}, vector) at phase 7 when deep convection was the strongest over the dateline. Reference vector shown at the top right corner of each panel. (a), (d), (g), and (j) are from the ERA-I/NOAA data; (b), (e), (h), and (k) are from the control coupled experiment C–30NS; and (c), (f), (i), and (l) are from the uncoupled experiment A–CTL.

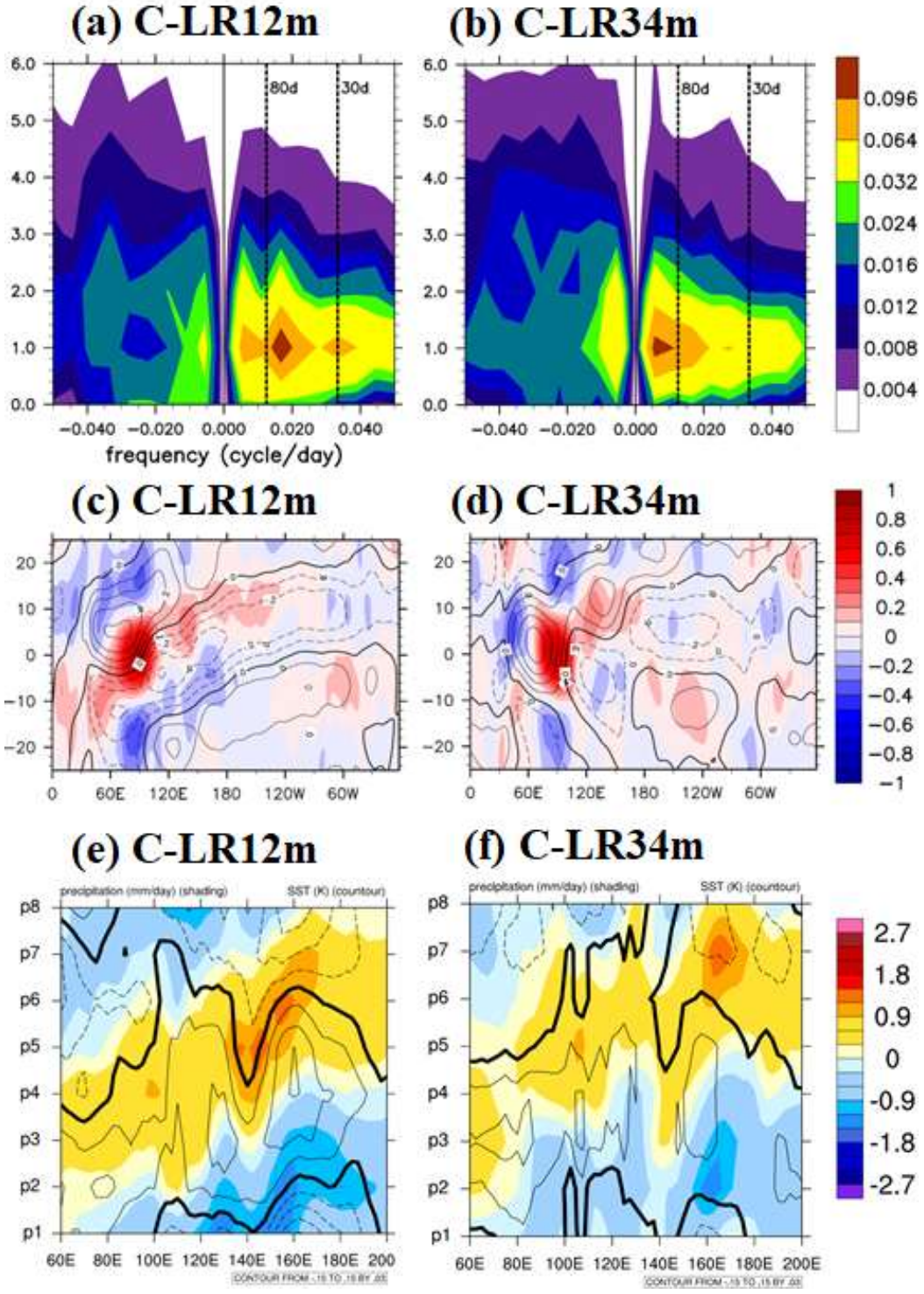

Figure 5. (a)–(b) Same as in Fig. 2(a) but for the C–LR12m and C–LR34m. (c)–(d) Same as in Fig. 2(d) but for the C–LR12m and C–LR34m. (e)–(f) Same as in Fig. 4(a) but for the C–LR12m and C–LR34m.

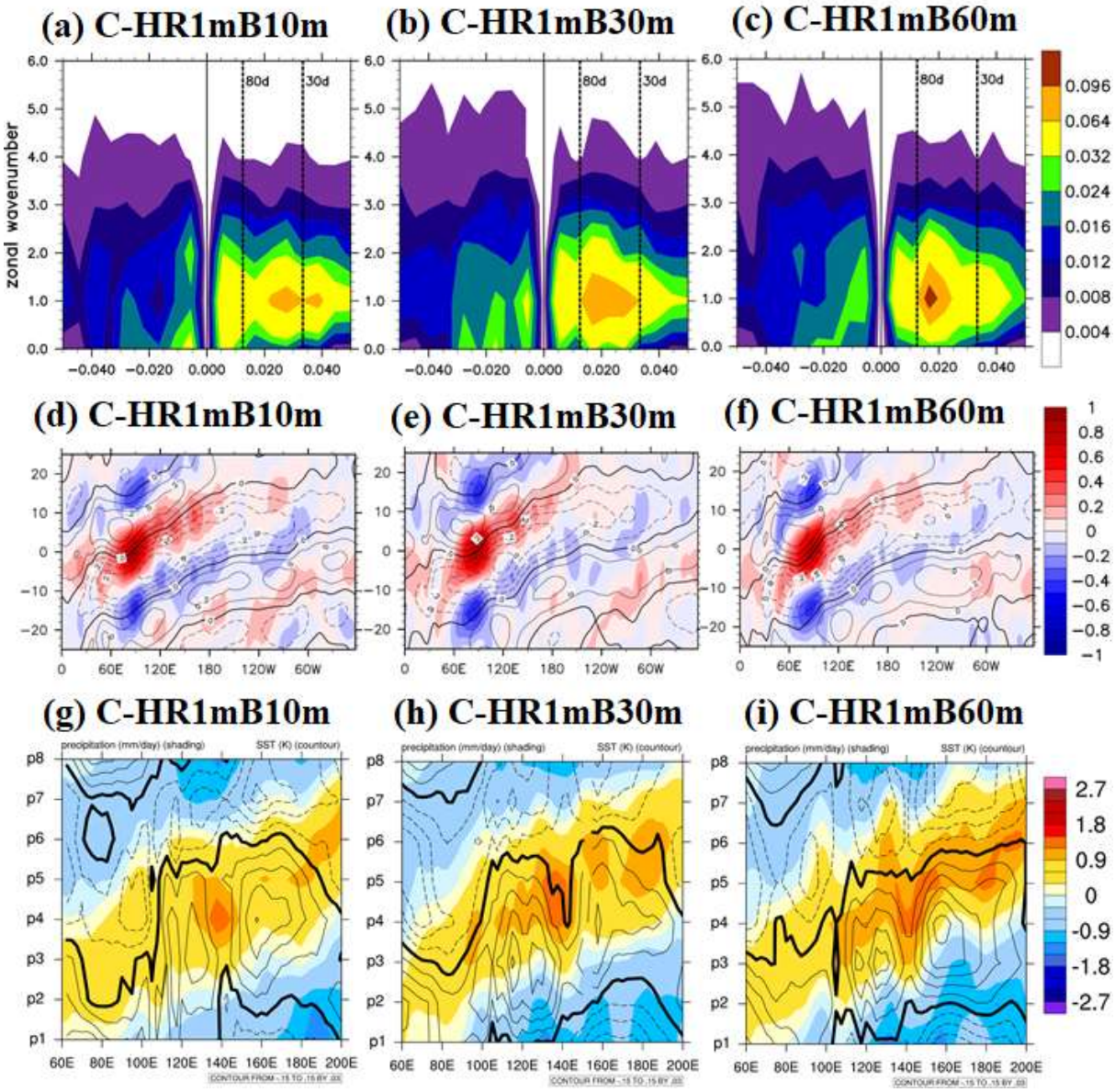

Figure 6. Same as in Fig. 5 but for the C–HR1mB10m, C–HR1mB30m, and C–HR1mB60m.

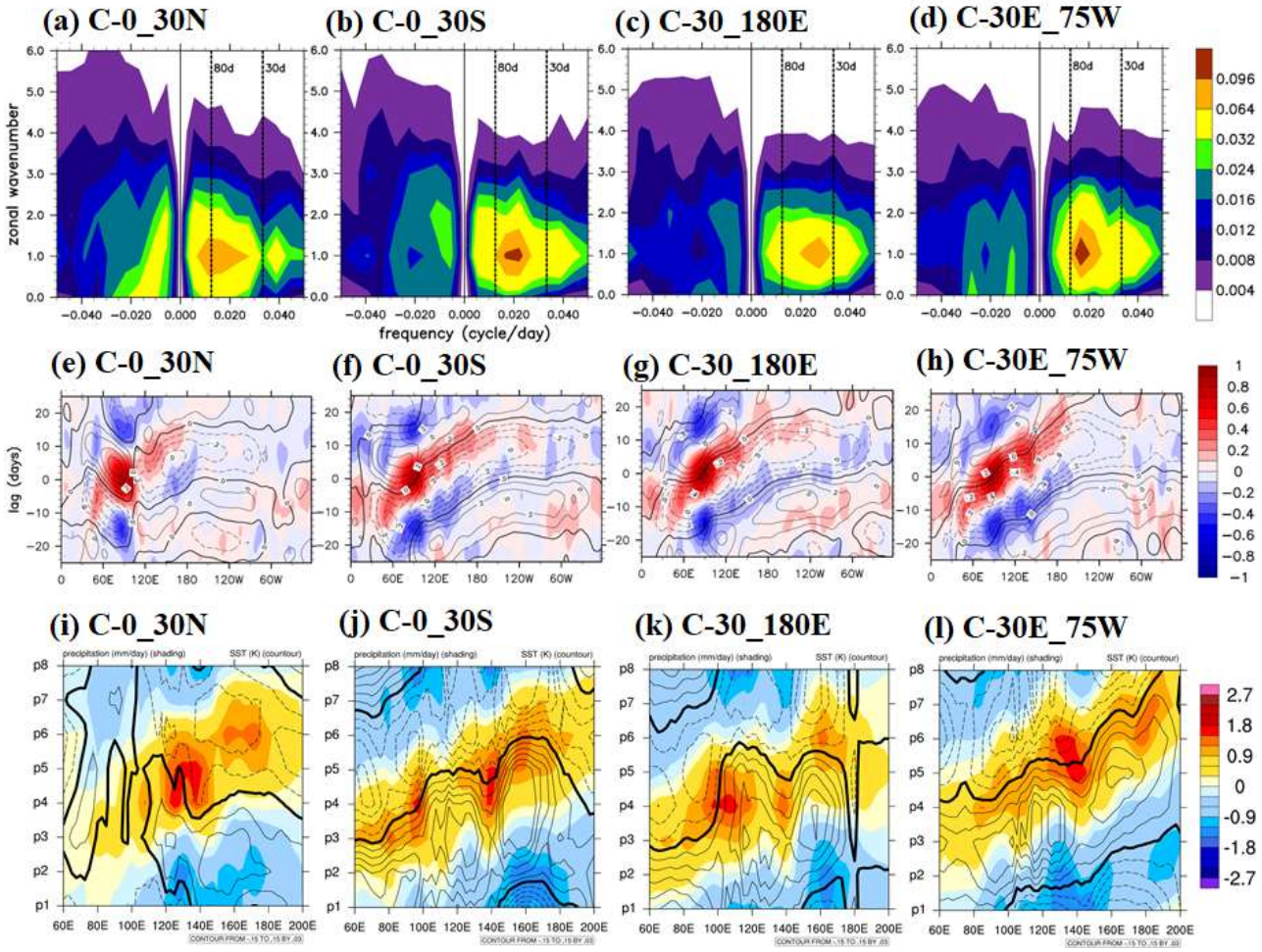

Figure 7. Same as in Fig. 5 but for the C–0_30N, C–0_30S, C–30_180E, and C–30E_75W.

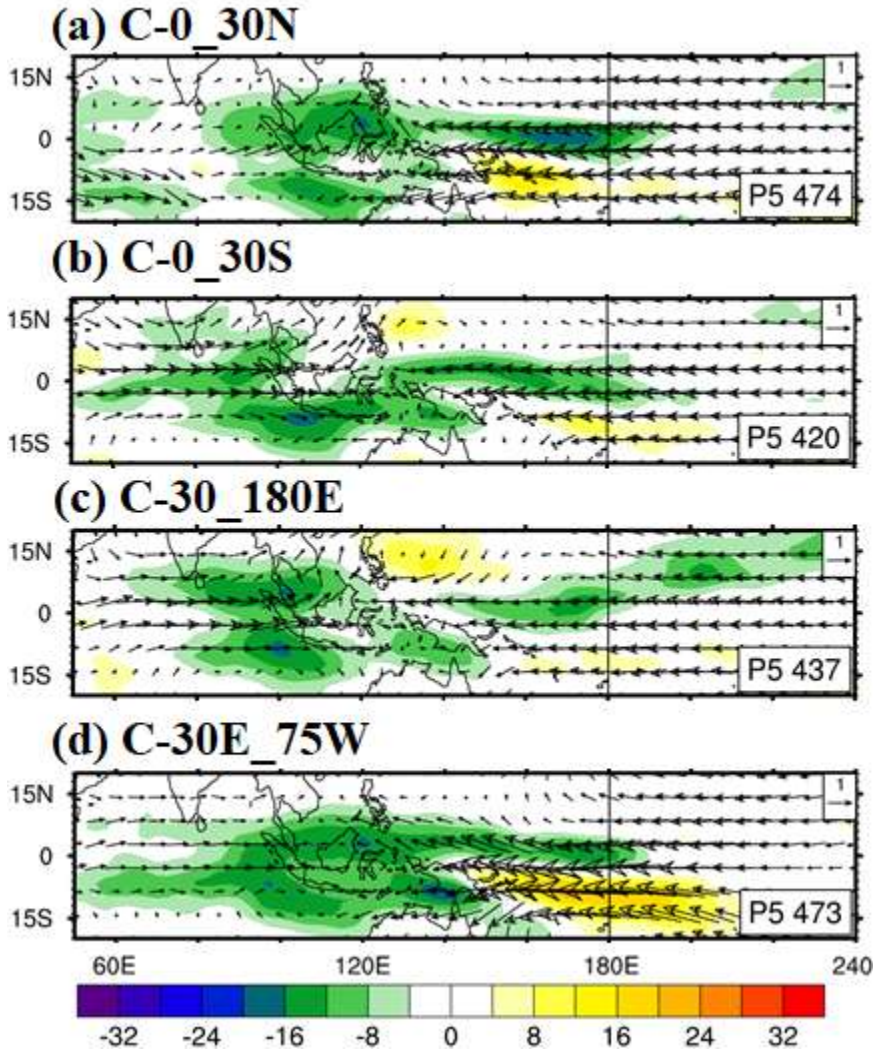

Figure 8. Same as in Fig. 3 but for phase 5 in the C–0_30N, C–0_30S, C–30_180E, and C–30E_75W.

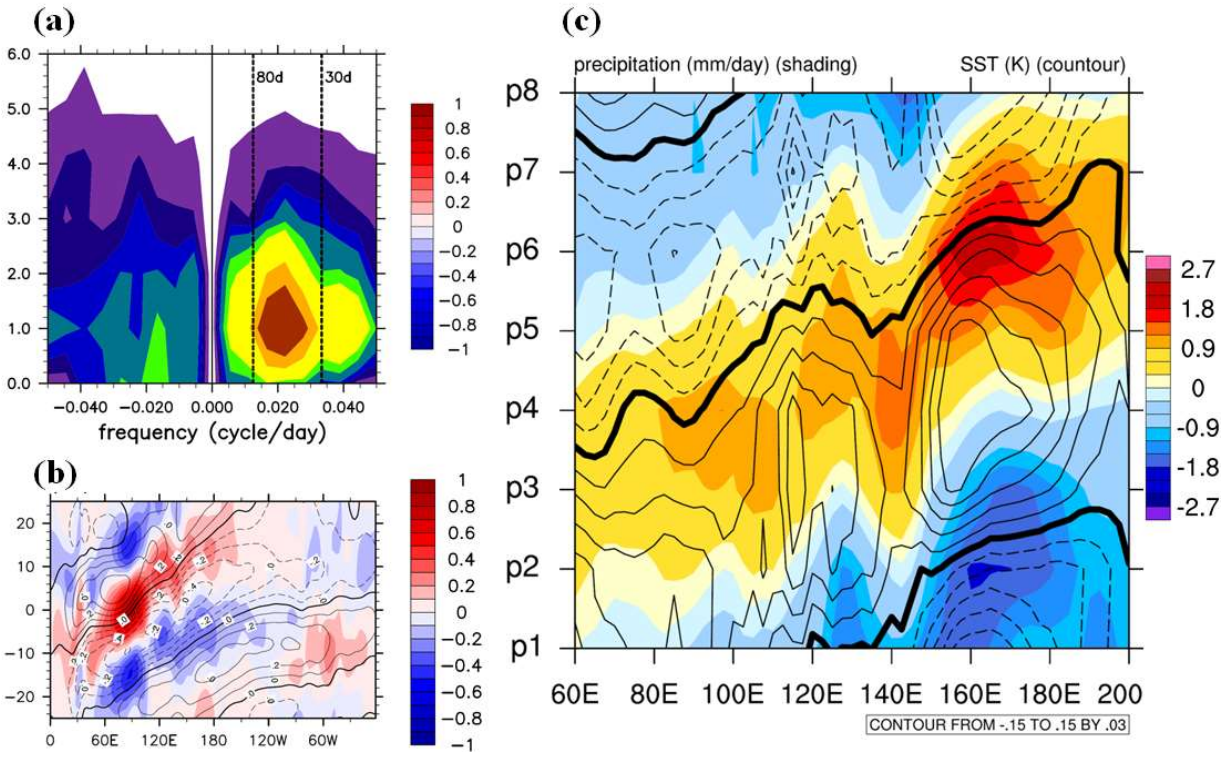

Figure 9. Similar as in Fig. 5 but for the C–30NS–nD.

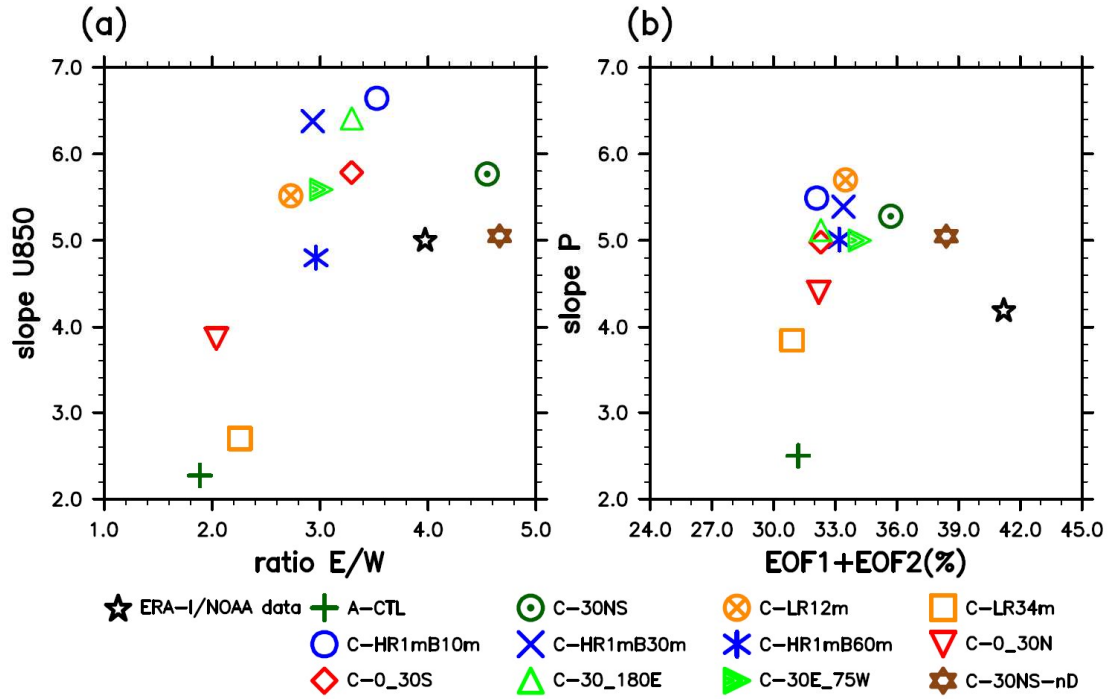

Figure 10. Scattered plots of various MJO indices in the ERA-I/NOAA data and 12 experiments: (a) power ratio of east/west propagating waves of wavenumber 1–3 of 850-hPa zonal winds (X-axis) with a 30–80-day period and eastward propagation speed of U850 anomaly (Y-axis) from the Hovmöller diagram and (b) RMM1 and RMM2 variance and eastward propagation speed of the filtered precipitation anomaly derived from the Hovmöller diagram.